

Geometric Decomposition of Statistical Inference through Gradient Flow and Co-Monotonicity Measures*

Pawel Gajer^{1†} and Jacques Ravel¹

¹University of Maryland School of Medicine

Abstract

Understanding feature-outcome associations in high-dimensional data remains challenging when relationships vary across subpopulations, yet standard methods assuming global associations miss context-dependent patterns, reducing statistical power and interpretability. We develop a geometric decomposition framework offering two strategies for partitioning inference problems into regional analyses on data-derived Riemannian graphs. Gradient flow decomposition uses path-monotonicity-validated discrete Morse theory to partition samples into gradient flow cells where outcomes exhibit monotonic behavior. Co-monotonicity decomposition leverages association structure: vertex-level coefficients measuring directional concordance between outcome and features, or between feature pairs, define embeddings of samples into association space. These embeddings induce Riemannian k-NN graphs on which biclustering identifies co-monotonicity cells (coherent regions) and feature modules. This extends naturally to multi-modal integration across multiple feature sets. Both strategies apply independently or jointly, with Bayesian posterior sampling providing credible intervals.

Keywords: geometric data analysis, gradient flow, co-monotonicity, Riemannian graphs, statistical inference, high-dimensional data, manifold learning, graph Laplacian, multiple testing, microbiome analysis

*Research reported in this publication was supported by grant number INV-048956 from the Gates Foundation.

†Corresponding author: pgajer@gmail.com

Software: The methods are implemented in the R package `gflow`, available at <https://github.com/pgajer/gflow>.

1. Introduction

Understanding which features associate with outcomes in high-dimensional data remains one of the central challenges in modern statistical analysis. Consider a microbiome study investigating spontaneous preterm birth [14, 11], where researchers measure hundreds of bacterial taxa across hundreds of samples. A particular phylotype might promote disease risk in women with one microbial community composition while showing no effect or even protective association in women with different community structures. Yet traditional correlation and regression methods that assume global, homogeneous relationships across all samples will average over these conflicting signals, potentially concluding that no association exists when in fact multiple distinct context-dependent mechanisms operate simultaneously.

This phenomenon of spatially heterogeneous associations appears throughout high-dimensional biomarker studies. In single-cell genomics, gene expression programs exhibit cell-type-specific relationships with outcomes [28]. In spatial transcriptomics, tissue architecture creates regions where the same molecular features play different functional roles [4]. In ecological data, species interactions vary across environmental gradients [19]. The common thread is that the ambient high-dimensional feature space contains subpopulations or regions where statistical relationships differ fundamentally, yet these regions are unknown a priori and must be discovered from data. When associations of opposite sign cancel in global analyses, investigators miss biologically meaningful mechanisms entirely, and the resulting models provide no basis for stratified interventions or personalized predictions.

What is needed, then, is a framework that naturally discovers the contextual structure latent in high-dimensional data and partitions the sample space into regions of homogeneous associative behavior. The partition itself should emerge from geometric properties of the data, which encode the complex interactions between features implicit in the ambient representation, rather than being imposed through arbitrary choices. By deconvoluting these hidden association patterns and making them explicit through geometric decomposition, the framework enables rigorous uncertainty quantification that respects both the spatial dependencies in graph-structured data and the exploratory nature of discovering structure and testing associations simultaneously.

A fundamental characteristic of high-dimensional data poses both challenge and opportunity: while datasets may contain hundreds or thousands of measured features, the underlying system often operates through far fewer degrees of freedom. Genomic studies measure tens of thousands of genes, yet cellular states often organize along a small number of developmental or functional axes [29]. Microbiome samples with hundreds of bacterial taxa concentrate near community type structures rather than filling the ambient space [22, 1]. Social network data with extensive demographic and behavioral variables frequently reduces to a handful of latent factors [17]. The manifold hypothesis [26, 13] formalizes this observation: high-dimensional data typically concentrates near low-dimensional manifolds embedded in the ambient feature space. While real data rarely forms smooth manifolds (exhibiting noise, stratification, and singular structures) the core insight remains valid that intrinsic dimensionality is far lower than nominal dimensionality, and that this geometric structure can be exploited for inference.

Geometric data analysis adopts a coordinate-free perspective, representing data through graphs or simplicial complexes that capture intrinsic relationships between samples. Rather than computing $E[Y|X]$ where $X \in \mathbb{R}^p$, we shift to computing $E[Y|G(X, y)]$ where $G(X, y)$ denotes a density-aware graph constructed from the predictor matrix X and observed response y . This reformulation makes the geometric structure explicit: statistical inference operates directly on the graph that encodes how samples relate to one another.

We work specifically with Riemannian graphs that possess rich local metric structure beyond simple edge weights. These graphs arise naturally from intersection k-nearest neighbor constructions interpreted through nerve complexes. Each vertex v corresponds to a sample, and the vertex mass $m_0(v)$ reflects the local density of samples in that region. Edges connect nearby samples, with edge masses $m_1(e)$ capturing the geometric extent of neighborhoods that share the edge. The Riemannian structure on the graph is encoded by the vertex mass matrix M_0 (diagonal, with entries $m_0(v)$) and the edge inner product matrix M_1 . While M_0 is determined by vertex masses alone, M_1 encodes more complex geometric relationships: beyond edge masses, it captures angular information between incident edges through inner products computed from the symmetrized graph Laplacian, defining a complete inner product structure on the space of edge chains [15]. The normalized graph Laplacian $L_{\text{norm}} = M_0^{-1/2} L_0 M_0^{-1/2}$, constructed from these masses, governs diffusion processes on the graph [8] and enables spectral filtering methods for signal recovery [25, 2].

Our approach builds fundamentally on Morse-Smale regression, introduced by Gerber et al. [16]. Their pioneering work brought ideas from Morse theory in differential topology [21, 30] into the statistical inference context, using gradient flow analysis to partition the feature space into cells determined by pairs of local extrema of the conditional expectation surface, then performing separate regression analyses within each cell. The framework elegantly connects differential topology with statistical practice, providing interpretable regional decompositions that respect the geometry of the prediction landscape. However, translating this continuous theory to the discrete, noisy setting of finite sample data presents several fundamental challenges. First, robust estimation of conditional expectations on graphs constructed from finite samples remains difficult. Moreover, even if the conditional expectation estimate were a smooth function, sampling it on a finite point set inevitably introduces spurious local extrema that do not correspond to genuine features of the underlying continuous function. Without methods to distinguish signal from noise in the extrema structure, the resulting cell decomposition may fragment the space unnecessarily or preserve spurious features. Second, real data-derived graphs typically contain long edges that connect distant points, creating basin jumping artifacts where gradient trajectories incorrectly cross between basins by following a single long edge rather than a path through intermediate samples.

Third, applying standard linear models within each gradient flow cell assumes that local linearity captures associations once heterogeneity is resolved through decomposition. However, even if relationships within cells are indeed locally linear, high-dimensional feature sets typically exhibit strong multicollinearity, with many features highly correlated with each other. Lasso-type regularization [27] can partially address this through automated feature selection, but different lasso variants handle correlated features in problematic ways: standard lasso tends to arbitrarily select one representative from a group of correlated features, while elastic net [31] includes entire groups but with potentially excessive shrink-

age. Moreover, if investigators wish to model how features interact with each other to influence outcomes, interaction terms must be pre-specified and included in the regression. With hundreds or thousands of features, the combinatorial explosion of potential interactions becomes computationally intractable and statistically underpowered [3, 12]. These challenges of multicollinearity, arbitrary feature selection, and unmodeled interactions suggest that alternative approaches to quantifying associations within cells may prove more robust than fitting linear models. Finally, the discrete-to-discrete translation requires careful treatment of the graph structure itself: working with mutual k-nearest neighbor graphs with simple edge weights may not capture the richer geometric structure that density-aware Riemannian metrics provide.

Our approach addresses these challenges while extending the Morse-Smale framework in two fundamental directions. Unlike variable selection or dimension reduction approaches that retain all samples while modifying the feature representation [27, 12, 26, 23], geometric decomposition stratifies the sample space itself into regions where different features may be relevant or where the same features operate through different mechanisms.

Figures 1 and 2 illustrate these concepts. Figure 1 demonstrates gradient-flow decomposition in one dimension, showing how a function with multiple local extrema naturally partitions into regions with homogeneous statistical behavior. Critical points (local minima and maxima) form boundaries defining ascending and descending basins, whose intersections create gradient-flow cells with monotonic behavior.

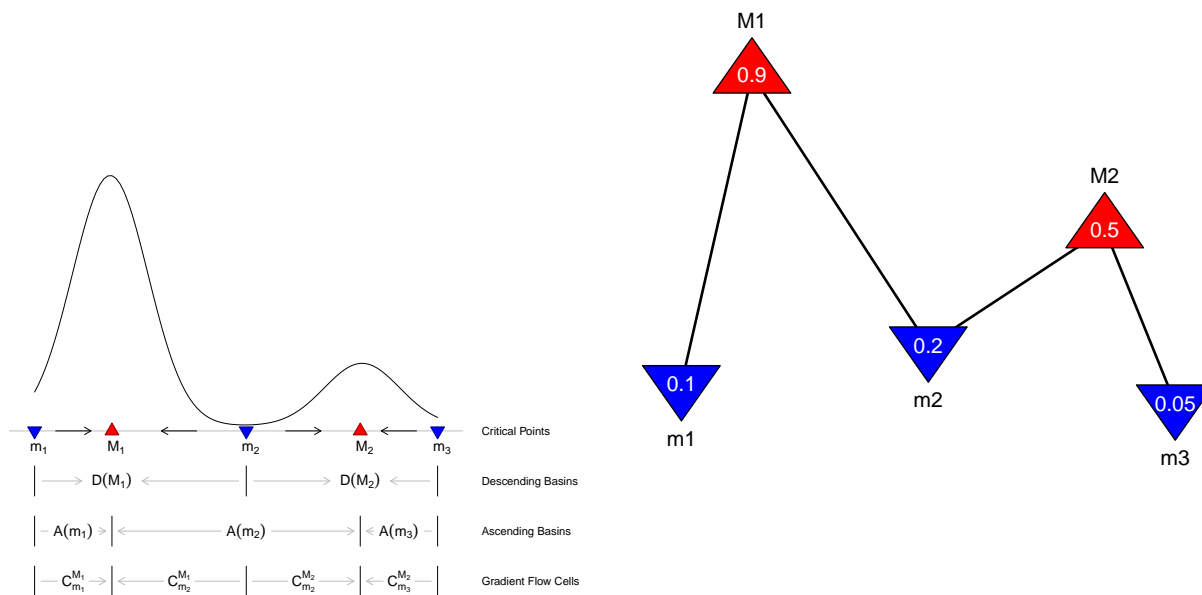


Figure 1: Domain decomposition via gradient flow. Panel A: One-dimensional function with local minima (m_1, m_2, m_3) and maxima (M_1, M_2), showing gradient directions and partitioning into ascending/descending basins and gradient flow cells. Panel B: Gradient flow graph with vertices as critical points (labeled with function values) and edges connecting minimum-maximum pairs, enabling monotonic statistical modeling within each cell.

The gradient flow graph serves as a one-dimensional skeleton capturing the essential shape of the prediction landscape, with edges representing natural non-linear generalizations of

principal directions in classical statistical methods. Figure 2 extends this framework to two dimensions, revealing additional complexities: non-trivial cell boundaries with irregular geometries, meaningful transition regions through saddle points, and the challenge of distinguishing statistically significant features from spurious patterns arising from finite sampling.

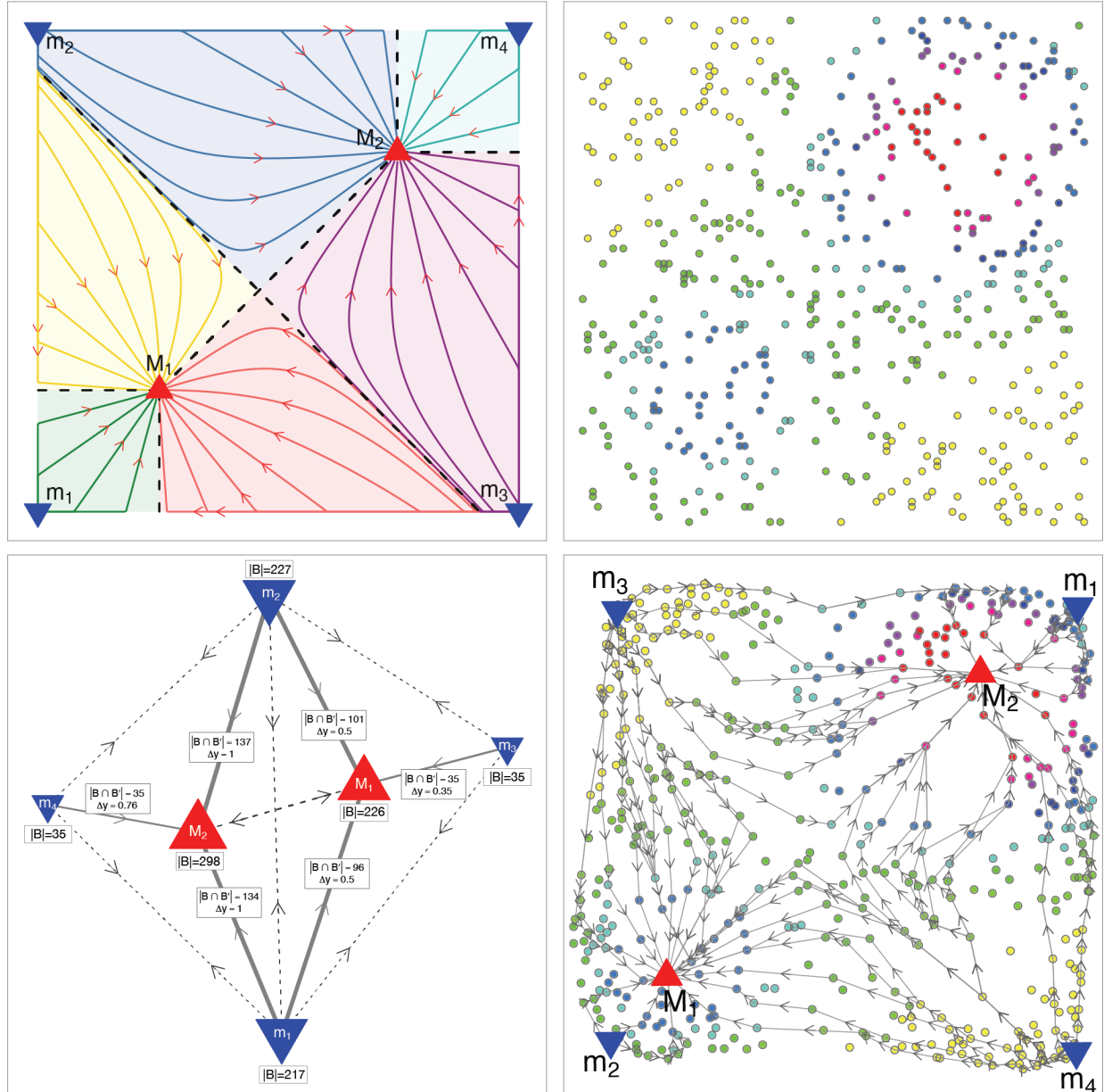


Figure 2: Gradient flow decomposition of a two-Gaussian mixture on $[0, 1]^2$. Top-left: Continuous function with critical points, gradient trajectories, and cell boundaries. Top-right: Random sample with color-coded function values. Bottom-right: k -nearest neighbor graph ($k = 36$) with selected gradient trajectories. Bottom-left: Gradient flow complex where solid edges connect minimum-maximum pairs and dashed edges represent minimum-minimum cells with saddle points; edges shown for cells with at least 25 points.

The first strategy employs gradient flow analysis to partition samples based on the geom-

etry of the outcome surface. Given a smoothed estimate $\hat{y} : V \rightarrow \mathbb{R}$ of the conditional expectation on graph vertices, we construct the discrete gradient flow by iteratively moving from each vertex toward neighbors with increasing (for ascending flow) or decreasing (for descending flow) function values. The trajectories of these flows partition vertices into basins of attraction: all vertices whose ascending flows terminate at the same local minimum belong to that minimum’s ascending basin, and similarly for descending flows toward local maxima. The intersections of ascending and descending basins define gradient flow cells $C(m, M) = B(m) \cap B(M)$ where the outcome function exhibits monotonic behavior. This construction realizes a discrete Morse-Smale complex on the graph, partitioning the sample space into regions where the outcome surface has uniform qualitative structure. We address the long edge problem through path monotonicity validation: for edges connecting distant points, we verify that the outcome function remains monotonic along the shortest alternative path. Only edges passing this validation participate in gradient flow computation, preventing basin jumping artifacts.

The second strategy emerged from considering how to quantify feature associations within gradient flow cells. Since the smoothed outcome \hat{y} exhibits monotonic behavior along gradient trajectories within each cell, a natural approach to identifying associated features would measure their monotonicity along these same trajectories. This path-based perspective, treating monotonicity as a functor of paths and individual functions, suggested an immediate generalization: rather than measuring single-function monotonicity along paths, we could measure co-monotonicity between pairs of functions, quantifying whether they vary together or oppositely along edges. A further abstraction yields vertex-level measures by aggregating edge-wise co-monotonicity over neighborhoods, producing coefficients that capture directional concordance locally while being independent of any particular path structure.

Co-monotonicity coefficients measure directional concordance between functions at individual graph vertices: for functions $y, z : V \rightarrow \mathbb{R}$, the coefficient at vertex v quantifies whether y and z tend to change together (positive co-monotonicity), opposite (negative), or independently (near zero) across edges incident to v . By computing co-monotonicity between an outcome y and features in a set $Z = \{z_1, \dots, z_m\}$, as well as between feature pairs, we obtain association profiles for each sample. Figure 3 illustrates these profiles in a microbiome application, where hierarchical clustering reveals coherent blocks of samples with similar association patterns and features with coordinated outcome relationships. These profiles define embeddings into association space, on which we construct k-nearest neighbor graphs and apply spectral biclustering [9, 18] to identify co-monotonicity cells—vertex regions and feature modules exhibiting coherent multivariate association patterns. Where gradient flow partitions based on how outcomes vary spatially, co-monotonicity partitioning discovers regions based on which features associate with outcomes and how features relate to each other. The framework extends naturally to multi-modal data integration, computing association matrices across feature sets and their cross-associations to construct embeddings that integrate information across modalities.

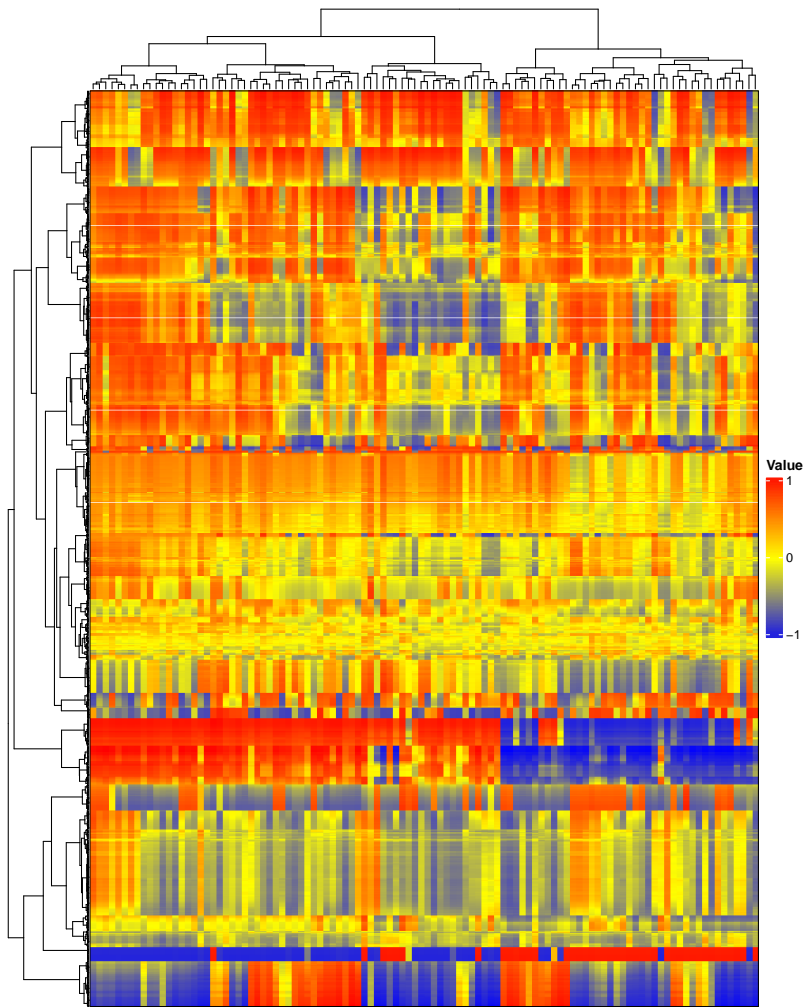


Figure 3: Co-monotonicity association profiles in vaginal microbiome data. Heatmap shows vertex-level co-monotonicity coefficients between spontaneous preterm birth outcome and bacterial phylotype abundances across samples from pregnant women (rows: samples, columns: phylotypes). Hierarchical clustering on both axes reveals coherent blocks: samples (rows) group by shared association patterns, while phylotypes (columns) cluster by co-varying relationships with the outcome. Red indicates positive co-monotonicity (phylotype and outcome increase together), blue indicates negative co-monotonicity (inverse relationship), and yellow indicates independence. The block structure demonstrates how biclustering on these association profiles identifies co-monotonicity cells—regions where specific feature modules exhibit consistent outcome associations.

The two strategies can be applied independently or jointly. Independent application suits exploratory analysis discovering structure from one perspective. Joint application enables assessment of concordance: do outcome-driven gradient flow cells align with association-driven co-monotonicity cells? High concordance suggests that regions of similar outcome values arise from consistent underlying mechanisms, while discordance indicates that similar outcomes can emerge through different pathways.

Our work extends Morse-Smale regression [16] through robust conditional expectation estimation on density-aware Riemannian graphs, systematic treatment of spurious extrema

through prominence filtering and basin overlap clustering, path monotonicity validation to resolve long edge artifacts, and co-monotonicity measures as alternatives to linear models within cells. Beyond these technical advances, our introduction of association-based decomposition through co-monotonicity complements Gerber’s outcome-based approach, providing a second lens for discovering structure.

The framework situates naturally within geometric data analysis rather than topological data analysis. While TDA [5, 10] emphasizes topological invariants like homology groups and persistence diagrams that remain unchanged under continuous deformations, GDA focuses on geometric properties like distances, angles, curvature, and geodesics that depend on the specific metric structure. Our Riemannian graphs with their vertex and edge masses capture local geometry that spectral methods can exploit for inference. The gradient flow we compute respects this geometry through derivative weighting in co-monotonicity coefficients and through the Riemannian metric implicit in the normalized Laplacian. This geometric emphasis connects our work more closely to manifold learning [26, 23, 8] and spectral graph theory [6, 20] than to persistent homology, though we acknowledge that the basin complex structure we compute has topological aspects.

From a statistical perspective, our geometric decomposition provides data-driven stratification for inference. Stratified sampling and stratified testing are well-established ideas in statistics [7], typically requiring investigators to specify strata based on known covariates. Our contribution is making stratification itself a geometric inference problem: the strata emerge from graph structure through gradient flow or co-monotonicity analysis rather than being predetermined. This connects to recent work on conditional independence testing [24] and context-specific associations, but grounds these ideas in explicit geometric partitions of the sample space.

The Bayesian inference framework we develop through posterior sampling on weighted Laplacians provides credible intervals that respect the geometry of the data manifold while enabling principled multiple testing corrections through the geometric structure of co-monotonicity cells.

Section 2 establishes the mathematical framework of Riemannian graphs, functions on graphs, and discrete gradient flow. Section 3 addresses the long edge problem through path monotonicity validation and presents basin computation algorithms. Section 4 introduces co-monotonicity coefficients, derives their properties, and develops matrix extensions for multivariate analysis. Section 5 establishes statistical inference procedures including vertex-wise permutation testing and Bayesian credible intervals via posterior sampling. Section 6 presents the geometric multiple testing framework through co-monotonicity cells and biclustering. Section 7 discusses computational implementation in the gflow R package. Section 8 concludes with discussion of limitations, relationships to other methods, and future directions.

2. Mathematical Framework: Riemannian Graphs and Discrete Gradient Flow

We begin with a question that motivates the entire geometric framework: given observations x_1, \dots, x_n in \mathbb{R}^d with associated outcomes y_1, \dots, y_n , how should we represent the inherent structure of the data in a way that enables both robust estimation of conditional expectations and natural stratification of the sample space? Standard approaches treat the data as points in Euclidean space, but this perspective obscures the crucial geometric relationships that determine how information should propagate between observations during inference.

2.1 From Point Clouds to Weighted Graphs

Consider a simple example. Suppose we observe ten points arranged in two clusters in the plane, with five points concentrated near $(0, 0)$ and five near $(1, 1)$. Traditional kernel methods place a Gaussian at each point and sum, yielding a smooth density estimate. Yet this approach treats all pairwise distances identically and fails to recognize that points within clusters share local geometry while points in different clusters do not, despite having similar distances to cluster boundaries.

The intersection k-nearest neighbor (ikNN) graph $G_k(X)$ associated with observations $X \subset \mathbb{R}^d$ provides a more geometric perspective. The vertices of $G_k(X)$ are all points X and two vertices x_i, x_j are connected by an edge if and only if $\hat{N}_k(x_i) \cap \hat{N}_k(x_j) \neq \emptyset$, where $\hat{N}_k(x_i)$ is the closed k-nearest neighbor ball of x_i , consisting of all k-nearest neighbors of x_i and the point x_i . For our two-cluster example with $k = 4$, edges connect points within each cluster but not across clusters (assuming sufficient separation). The graph structure reveals the discrete geometry: the two clusters appear as connected components, and any function defined on vertices can diffuse within components but not between them.

However, unweighted graphs lose important information. In regions where points lie densely, small Euclidean distances separate neighbors, while in sparse regions, large distances occur. A single long edge might connect distant points creating an artificial bridge that permits gradient flow to jump between geometrically distant regions. We require vertex and edge weights that encode both local density and geometric scale.

2.2 Riemannian Structure Through Mass Assignment

We construct a Riemannian graph through systematic assignment of masses to vertices and edges. The vertex mass $m_0(v)$ at vertex v quantifies the local concentration of observations, while edge masses $m_1(e)$ measure geometric relationships between neighborhoods. These masses induce a complete metric structure on the graph, enabling precise measurement of distances, angles, and volumes.

Let $\mathcal{U} = \{\hat{N}_k(x_1), \dots, \hat{N}_k(x_n)\}$ be the kNN balls covering of $X = \{x_1, x_2, \dots, x_n\}$. The nerve complex of this covering has vertices corresponding to observations, with simplices recording multi-way neighborhood intersections. We focus on the 1-skeleton (vertices and

edges), which forms a graph where an edge $[i, j]$ exists whenever $\hat{N}_k(x_i) \cap \hat{N}_k(x_j) \neq \emptyset$. Thus, the intersection k-nearest neighbor graph is the 1-skeleton of the nerve complex of the k-nearest neighbor covering.

The vertex mass $m_0(i)$ represents the measure of the neighborhood $\hat{N}_k(x_i)$. In practice, we use density-surrogate weights

$$m_0(i) = w(x_i) = (\varepsilon + d_k(x_i))^{-\alpha} \quad (1)$$

where $d_k(x_i)$ denotes the distance from x_i to its k -th nearest neighbor, $\varepsilon > 0$ is a small regularization constant, and $\alpha \in [1, 2]$ controls the degree of density weighting. The vertex masses are normalized so that $\sum_{i=1}^n m_0(i) = n$.

The formula inverts neighborhood radius: points in dense regions have small d_k and receive large mass, while isolated points have large d_k and receive small mass. The exponent α modulates sensitivity to density variation. Alternative formulations using exponential or rational kernels provide smooth density dependence.

For an edge $e = [i, j]$, the edge mass $m_1(e)$ equals the total vertex mass in the neighborhood intersection:

$$m_1([i, j]) = \sum_{\ell: x_\ell \in \hat{N}_k(x_i) \cap \hat{N}_k(x_j)} m_0(\ell). \quad (2)$$

For two edges $e_{ij} = [i, j]$ and $e_{is} = [i, s]$ sharing vertex i , their inner product equals the triple intersection mass:

$$\langle e_{ij}, e_{is} \rangle = \sum_{\ell: x_\ell \in \hat{N}_k(x_i) \cap \hat{N}_k(x_j) \cap \hat{N}_k(x_s)} m_0(\ell). \quad (3)$$

Thus, e_{ij}, e_{is} are orthogonal if and only if

$$\hat{N}_k(x_i) \cap \hat{N}_k(x_j) \cap \hat{N}_k(x_s) = \emptyset$$

assuming $m_0(x_i) > 0$ for all x_i .

These inner products encode geometric relationships beyond simple edge weights. Two edges sharing a vertex are orthogonal if their corresponding neighborhoods intersect trivially, while edges with large triple intersection mass form acute angles. The collection of all edge inner products assembles into the edge mass matrix M_1 , with diagonal entries $M_1(e, e) = m_1(e)$ and off-diagonal entries $M_1(e_{ij}, e_{is}) = \langle e_{ij}, e_{is} \rangle$.

We encode the vertex masses in a diagonal matrix $M_0 = \text{diag}(m_0(1), \dots, m_0(n))$. The pair (M_0, M_1) constitutes the Riemannian structure, determining inner products on the spaces of vertex chains C_0 and edge chains C_1 .

2.3 The Graph Laplacian and Diffusion

The Riemannian structure determines a graph Laplacian that governs diffusion on the weighted graph. We begin with the boundary operator $B_1 : C_1 \rightarrow C_0$, which maps edge

chains to vertex chains according to

$$(B_1\alpha)(i) = \sum_{j \in N(i)} (\alpha([j, i]) - \alpha([i, j])),$$

where $N(i)$ denotes the neighborhood of vertex i and $[i, j]$ denotes the oriented edge from i to j . This operator encodes the graph's combinatorial structure through the vertex-edge incidence relations.

We define the graph Laplacian using edge conductances derived from the edge mass matrix. For each edge e , we set the conductance $c_e = m_1(e)$, using the edge mass directly. Since the base measure $m_0(i) = (\varepsilon + d_k(x_i))^{-\alpha}$ already inverts local scales, edges in dense regions naturally receive large conductances while edges in sparse regions receive small conductances. Assembling these into a diagonal matrix $C = \text{diag}(c_1, \dots, c_m)$, we construct the unnormalized Laplacian

$$L_{\text{div}} = B_1 C B_1^T.$$

This operator is symmetric and positive semidefinite, with eigenvalues encoding the graph's connectivity structure.

For computational purposes, we work with the symmetrized normalized Laplacian

$$L_{\text{norm}} = M_0^{-1/2} L_{\text{div}} M_0^{-1/2},$$

which has eigenvalues in $[0, 2]$ and admits spectral decomposition through standard symmetric eigensolvers. The normalization by vertex masses balances the influence of vertices with different local densities, preventing high-degree vertices from dominating the diffusion process.

The heat equation $\partial\rho/\partial t = -L_{\text{div}}\rho$ describes how vertex masses evolve under diffusion. The solution $\rho(t) = \exp(-tL_{\text{div}})\rho(0)$ applies the heat kernel to the initial distribution. For small t , diffusion smooths local irregularities while preserving global structure; for large t , all mass flows toward the stationary distribution. The Riemannian structure determines diffusion rates: edges with large mass (small Riemannian length) facilitate rapid exchange, while edges with small mass (large Riemannian length) impede flow.

The edge mass matrix M_1 contains not only diagonal entries $m_1(e)$ but also off-diagonal entries encoding inner products between edges sharing vertices through triple neighborhood intersections. In the Laplacian construction above, we use only the diagonal structure for computational efficiency. The full Riemannian geometry, including these off-diagonal terms, is incorporated in the gradient computation used for basin analysis (Section 3), where it plays a crucial role in determining flow directions. Extending the Laplacian construction to utilize the complete M_1 structure remains an important direction for future work.

2.4 Functions on Graphs and the Discrete Gradient

We consider real-valued functions $f : V \rightarrow \mathbb{R}$ defined on graph vertices. Such functions represent observed outcomes, fitted predictions, or any other vertex-associated quantities. The gradient of f measures how the function changes across edges.

The gradient operator $\nabla f : E \rightarrow \mathbb{R}$ assigns to each oriented edge a value encoding the directional rate of change of f . The Riemannian structure determines this assignment through the adjoint of the boundary operator. Formally, the gradient is defined by the relation

$$\langle B_1 \phi, f \rangle_{M_0} = \langle \phi, \nabla f \rangle_{M_1}$$

for all edge functions ϕ and vertex functions f , where the left side uses the vertex inner product weighted by M_0 and the right side uses the edge inner product weighted by M_1 . This yields $\nabla f = B_1^*(f)$, where $B_1^* : C_0 \rightarrow C_1$ denotes the adjoint operator.

In the diagonal case, where edges are orthogonal in the Riemannian metric (meaning M_1 is diagonal with $M_1(e_{ij}, e_{is}) = 0$ for distinct edges sharing a vertex), the gradient has an explicit formula. For an edge $e = [i, j]$ directed from vertex i to vertex j , we have

$$(\nabla f)(e) = \frac{m_0(j)f(j) - m_0(i)f(i)}{m_1(e)},$$

where the vertex masses in the numerator weight the function values according to local density, and the edge mass in the denominator normalizes by the geometric scale of the neighborhood intersection.

This formula admits a natural interpretation. In regions where both vertices have equal mass (uniform density), the gradient reduces to the function difference divided by edge mass, analogous to a directional derivative where edge mass acts as effective distance. In non-uniform regions, vertices with larger mass contribute more strongly, reflecting that these vertices represent denser neighborhoods where the function value carries greater statistical weight. The division by edge mass ensures that the gradient measures rate of change per unit geometric distance rather than absolute difference.

When the full non-diagonal structure of M_1 is employed (incorporating off-diagonal entries from triple neighborhood intersections), computing $\nabla f = B_1^*(f)$ requires solving the linear system $M_1 x = B_1^T M_0 f$, which we address through iterative methods in the basin analysis of Section 3.

2.5 Spectral Filtering and Conditional Expectation Estimation

Given observed outcomes y_1, \dots, y_n , we estimate the conditional expectation $E[Y|X]$ through spectral filtering on the graph Laplacian. The empirical vertex function $y = (y_1, \dots, y_n)$ contains both signal (the true conditional expectation) and noise. Spectral methods decompose y into components corresponding to different geometric frequencies on the graph.

We begin with the eigendecomposition $L_{\text{norm}} = V \Lambda V^T$, where Λ is diagonal with eigenvalues $0 = \lambda_1 \leq \lambda_2 \leq \dots \leq \lambda_n \leq 2$ and V contains the corresponding eigenvectors. The eigenvector v_1 associated with $\lambda_1 = 0$ is constant (proportional to $M_0^{1/2} \mathbf{1}$), while eigenvectors associated with small positive eigenvalues vary slowly across edges, and eigenvectors with large eigenvalues oscillate rapidly.

The smoothed estimate takes the form

$$\hat{y} = \sum_{i=1}^n h(\lambda_i) \langle y, v_i \rangle v_i, \tag{4}$$

where $h : [0, 2] \rightarrow [0, 1]$ is a spectral filter that attenuates high-frequency components. We employ the heat kernel filter $h(\lambda) = \exp(-t\lambda)$, which corresponds to solving the heat equation for time t :

$$\hat{y} = \exp(-tL_{\text{norm}})y. \quad (5)$$

The diffusion time t controls smoothness: small t yields estimates close to the empirical values, while large t produces heavily smoothed estimates. We select t through generalized cross-validation or by monitoring convergence of the gradient flow structure: we increase t until the number and prominence of local extrema stabilize.

This spectral approach has several advantages over local smoothing methods. It naturally adapts to the graph geometry, diffusing rapidly within well-connected regions and slowly across sparse connections. It respects the Riemannian structure encoded in M_0 and M_1 , ensuring that smoothing follows the intrinsic manifold rather than the ambient Euclidean space. It enables efficient computation through sparse matrix methods and iterative eigensolvers, scaling to graphs with thousands of vertices.

3. The Long Edge Problem and Path Monotonicity Validation

Real data-derived graphs pose a fundamental challenge for discrete gradient flow computation: the k-nearest neighbor construction that makes the graph computationally tractable simultaneously introduces edges that violate the geometric principles underlying gradient trajectories. We confront the question of why naive gradient flow fails on realistic graphs and develop a path-based validation criterion that restores geometric faithfulness without requiring expensive global computations.

3.1 The Challenge of Long Edges

Consider constructing a k-nearest neighbor graph from a sample drawn from a low-dimensional manifold embedded in high-dimensional space. When the manifold curves or has boundaries, points that are close in Euclidean distance may lie far apart along the manifold. A point near the edge of a curved region might have as its k-th nearest neighbor a point on the opposite side of a valley, leading to an edge that shortcuts across the manifold rather than following its intrinsic geometry.

These long edges are necessary for graph connectivity. Without them, the graph fragments into components corresponding to dense regions, preventing paths between different parts of the sample. Yet these same edges can create artifacts in gradient flow computation. Consider a vertex v in a descending basin of a local minimum m , where the smoothed function \hat{y} decreases monotonically along all paths through neighboring vertices toward m . If v has a long edge to a vertex u in a different basin where $\hat{y}(u) < \hat{y}(v)$, the naive gradient rule (follow the neighbor with minimal function value) directs the trajectory to jump across basins, violating the fundamental property that gradient flow should follow monotone paths along the underlying geometry.

3.2 Inadequacy of Existing Approaches

One might attempt to resolve this issue through more sophisticated gradient computation. For basin analysis, we can compute the discrete gradient incorporating the full Riemannian structure via

$$(\nabla y)_e = [M_1^{-1} B_1^T M_0 y]_e,$$

where $B_1 : \mathbb{R}^E \rightarrow \mathbb{R}^V$ is the boundary operator, M_0 is the vertex mass matrix, and M_1 is the full edge mass matrix including off-diagonal entries encoding geometric relationships between edges sharing vertices (see Appendix). This gradient accounts for global geometric structure beyond local function differences.

However, even this sophisticated gradient computation does not resolve the long edge problem. The gradient formula incorporates edge masses that quantify neighborhood overlaps, but the fundamental issue remains: a long edge connecting vertices in different basins can still produce a gradient that directs flow across basin boundaries, even when the edge has appropriately small mass. The problem is not that the gradient is computed incorrectly, but that the graph topology itself contains edges that violate the manifold geometry. No local gradient computation can distinguish between a long edge that shortcuts across a valley (problematic) versus one that legitimately connects distant points along a genuine gradient path (acceptable).

Alternatively, one might restrict gradient flow to edges shorter than a quantile threshold τ_q , where τ_q is the q -quantile of the edge length distribution for some $q \in [0.5, 1]$. This heuristic removes the most problematic edges but discards potentially valid geometric information. A long edge might legitimately connect vertices that lie on a genuine gradient trajectory if the underlying function varies smoothly between them. Uniform length thresholding cannot distinguish between geometrically faithful long edges and artifactual ones, leading to unnecessary loss of connectivity and potential fragmentation of basins.

What we need instead is a criterion that validates each edge based on the actual function behavior along paths, not merely on edge length or local gradient values. This motivates our path monotonicity approach.

3.3 Path Monotonicity as a Validation Criterion

We return to the defining property of gradient trajectories in smooth Morse theory. Let $f : M \rightarrow \mathbb{R}$ be a smooth function on a Riemannian manifold M , and let $\gamma : [0, 1] \rightarrow M$ be a gradient flow trajectory with $\gamma(0) = p$ and $\gamma(1) = q$. For ascending flow, $\gamma'(t) = +\nabla f(\gamma(t))$; for descending flow, $\gamma'(t) = -\nabla f(\gamma(t))$. In both cases, the function varies monotonically along γ . For ascending trajectories:

$$\frac{d}{dt} f(\gamma(t)) = \langle \nabla f(\gamma(t)), \gamma'(t) \rangle = \|\nabla f(\gamma(t))\|^2 > 0,$$

while for descending trajectories, the derivative has the opposite sign. The key property is that f changes monotonically along the entire path, assuming γ does not pass through critical points. This monotonicity is not merely a local property at each point but a global constraint on the trajectory.

In the discrete setting, we translate this insight into an operational criterion. For an edge $e = [i, j]$ to participate in gradient flow, we require not only that the function increases from i to j (for ascending flow) but that the increase reflects genuine geometric variation rather than artificial jumping across the manifold. We validate this by examining alternative paths: if the function truly varies smoothly in the region containing i and j , then the shortest path connecting them should exhibit consistent monotonic behavior.

Let $\gamma = (v_0, v_1, \dots, v_k)$ be a path in G with $v_0 = i$ and $v_k = j$. The function \hat{y} is monotone along γ if for all $\ell \in \{0, 1, \dots, k-1\}$ we have $\hat{y}(v_{\ell+1}) > \hat{y}(v_\ell)$ for ascending monotonicity, or $\hat{y}(v_{\ell+1}) < \hat{y}(v_\ell)$ for descending monotonicity. We quantify the degree of monotonicity through the co-monotonicity coefficient along the path:

$$\text{cm}(\hat{y}; \gamma) = \frac{\sum_{\ell=0}^{k-1} w_{v_\ell v_{\ell+1}} \Delta_{v_\ell v_{\ell+1}} \hat{y}}{\sum_{\ell=0}^{k-1} w_{v_\ell v_{\ell+1}} |\Delta_{v_\ell v_{\ell+1}} \hat{y}|},$$

where $\Delta_{v_\ell v_{\ell+1}} \hat{y} = \hat{y}(v_{\ell+1}) - \hat{y}(v_\ell)$ and $w_{v_\ell v_{\ell+1}}$ are edge weights. $\text{cm}(\hat{y}; \gamma) = 1$ for \hat{y} strictly ascending along γ and $\text{cm}(\hat{y}; \gamma) = -1$ for \hat{y} strictly descending along γ .

The path co-monotonicity coefficient aggregates signed differences along the path, normalized by total variation. Perfect monotonicity yields $\text{cm}(\hat{y}; \gamma) = \pm 1$, while oscillating functions produce values closer to zero. We employ this coefficient to define a validation procedure for long edges.

For an edge $e = [i, j]$ with edge length Δ_e exceeding a threshold τ_q (typically the q -quantile of edge lengths for $q \in [0.75, 0.90]$), we compute the shortest path $\gamma_{[i,j]}$ from i to j in the graph $G \setminus \{e\}$ (after temporarily removing edge e). If no such path exists, the edge is essential for connectivity and we accept it by default. If $\gamma_{[i,j]}$ exists, we evaluate $\text{cm}(\hat{y}; \gamma_{[i,j]})$ and compare against a threshold $\theta \in [0.85, 1.0]$. For ascending flow, we require $\text{cm}(\hat{y}; \gamma_{[i,j]}) \geq \theta$; for descending flow, $\text{cm}(\hat{y}; \gamma_{[i,j]}) \leq -\theta$. The edge participates in gradient flow only if this monotonicity condition holds.

Given a function $\hat{y} : V \rightarrow \mathbb{R}$, a quantile threshold q , and a monotonicity threshold θ , the validated edge set for ascending flow is

$$E_{\text{val}}^\uparrow = \{[i, j] \in E : \hat{y}(j) > \hat{y}(i) \text{ and } (\Delta_e \leq \tau_q \text{ or } \mathcal{V}^\uparrow(e))\},$$

where $\mathcal{V}^\uparrow(e)$ holds if either no path from i to j exists in $G \setminus \{e\}$, or the shortest such path $\gamma_{[i,j]}$ satisfies $\text{cm}(\hat{y}; \gamma_{[i,j]}) \geq \theta$. Similarly, for descending flow:

$$E_{\text{val}}^\downarrow = \{[i, j] \in E : \hat{y}(j) < \hat{y}(i) \text{ and } (\Delta_e \leq \tau_q \text{ or } \mathcal{V}^\downarrow(e))\},$$

where $\mathcal{V}^\downarrow(e)$ holds if either no path from i to j exists in $G \setminus \{e\}$, or $\text{cm}(\hat{y}; \gamma_{[i,j]}) \leq -\theta$. We compute gradient trajectories using only edges in E_{val}^\uparrow for ascending basins and $E_{\text{val}}^\downarrow$ for descending basins.

This criterion captures the essential geometric property of gradient trajectories while remaining computationally tractable. Computing the shortest path in $G \setminus \{e\}$ requires breadth-first search, an $O(|E|)$ operation for sparse graphs. Evaluating path monotonicity involves a single pass through the path vertices, adding negligible overhead. The total cost of validating all long edges is $O(L \cdot |E|)$ where L is the number of long edges, typically a small fraction of $|E|$ for well-chosen q .

3.4 Local Extrema and Spurious Feature Removal

We return to a fundamental question that arises whenever discrete Morse theory is applied to finite samples from continuous manifolds: how should we distinguish genuine features of the underlying geometry from artifacts introduced by discretization and statistical estimation? The gradient flow structure computed from path-validated edges naturally partitions the graph into basins of attraction, with each basin containing vertices that flow to a common local extremum. However, not all local extrema identified by this purely combinatorial criterion represent meaningful features of the conditional expectation function. Some extrema arise from sampling variability, others from numerical artifacts in the smoothing process, and still others from the discretization itself, where the restriction of a smooth function to graph vertices inevitably creates spurious critical points that do not correspond to extrema of the continuous function.

Consider first the geometric origin of spurious extrema. Let $f : M \rightarrow \mathbb{R}$ be a smooth function on a Riemannian manifold M , and let $X = \{x_1, \dots, x_n\}$ be a finite sample from M . The restriction $y = f|_X$ defines a function on the sample points, which we represent as a function on the vertices of the graph $G_k(X)$ derived from the k -nearest neighbor construction. Even when f has only a small number of critical points on M , the discrete function y typically exhibits numerous local extrema on $G_k(X)$. This phenomenon occurs because discrete extrema are defined purely by local comparisons: a vertex v is a local minimum if $y(v) < y(u)$ for all neighbors $u \in N(v)$, and a local maximum if $y(v) > y(u)$ for all $u \in N(v)$. The graph structure imposes a specific neighborhood system that may not align with the natural neighborhoods in the continuous manifold, leading to vertices that satisfy the discrete extremum condition despite lying on smooth portions of the function landscape.

After spectral smoothing to estimate the conditional expectation, additional spurious extrema can emerge from the interplay between the smoothing operator and the graph geometry. The heat kernel filter $\exp(-tL_{\text{norm}})$ diffuses function values across edges, with diffusion rates determined by the Riemannian structure. In regions where the graph locally approximates the manifold geometry well, smoothing faithfully reconstructs the underlying smooth function. However, in regions where long edges bridge across valleys or where local density variations create anomalous mass distributions, the smoothed function may develop local extrema that reflect these geometric artifacts rather than true features of the conditional expectation.

We address this challenge through a systematic refinement pipeline that progressively removes spurious extrema based on multiple geometric and statistical criteria. The refinement process operates in stages, each targeting a different source of spuriousness while preserving the structure of the function landscape.

The first filtering stage removes extrema whose function values are insufficiently distinct from the global mean. We compute the relative value $r(v) = \hat{y}(v)/\bar{y}$ for each extremum vertex v , where $\bar{y} = n^{-1} \sum_{i=1}^n y(i)$ denotes the mean of y across all vertices. For local maxima, we retain only those satisfying $r(v) \geq \rho_{\max}$ for a threshold $\rho_{\max} > 1$ (typically $\rho_{\max} \in [1.1, 1.5]$), while for local minima we require $r(v) \leq \rho_{\min}$ with $\rho_{\min} < 1$ (typically $\rho_{\min} \in [0.5, 0.9]$). These thresholds focus subsequent analysis on prominent features that

rise substantially above or descend significantly below the average function level. Extrema failing these criteria represent minor fluctuations that, while formally satisfying the local comparison condition, lack sufficient magnitude to warrant interpretation as distinct features of the conditional expectation surface.

The second stage addresses redundancy arising from multiple nearby extrema representing the same underlying feature. We quantify similarity between extrema through their basin overlap. For two basins A_i and A_j with vertex sets V_i and V_j , the overlap coefficient is defined as

$$\omega(A_i, A_j) = \frac{|V_i \cap V_j|}{\min(|V_i|, |V_j|)}, \quad (6)$$

which measures what fraction of the smaller basin’s vertices are shared with the larger basin. This asymmetric measure emphasizes cases where one basin is substantially contained in another, indicating that the corresponding extrema likely represent the same feature at different scales of resolution. We construct an overlap graph where vertices correspond to extrema of the same type (all maxima or all minima), and we add an edge between extrema i and j whenever $\omega(A_i, A_j) \geq \omega_{\text{thld}}$ for a threshold $\omega_{\text{thld}} \in [0.10, 0.20]$. Connected components in this overlap graph identify clusters of similar extrema. Within each cluster, we merge the basins by retaining only the extremum with the most extreme function value (highest for maxima, lowest for minima) and assigning all vertices in the cluster’s combined basin to this representative extremum. This consolidation reduces redundancy while preserving the essential gradient flow structure, as vertices in merged basins still flow toward genuine extrema, just through a simplified representative structure.

The third stage removes extrema whose basins exhibit geometric characteristics suggesting isolation artifacts or boundary effects. We compute two complementary measures of basin geometry for each extremum. The first is the mean hop- k distance, which quantifies extended neighborhood isolation. For an extremum at vertex v , we identify all vertices $U_k(v)$ at graph distance exactly k from v through breadth-first search, then compute the mean geodesic distance

$$d_k(v) = \frac{1}{|U_k(v)|} \sum_{u \in U_k(v)} d_G(v, u), \quad (7)$$

where $d_G(v, u)$ denotes the length of the shortest path from v to u in the metric graph. This measure captures whether the extremum lies in a locally sparse or dense region at scale k (typically $k = 2$ or $k = 3$). High values of $d_k(v)$ indicate that vertices at hop distance k are geometrically far from v , suggesting the extremum sits in an isolated or boundary region.

The second geometric measure is the effective degree $\text{deg}_{\text{eff}}(v)$, defined as the sum of density-surrogate weights over all neighbors:

$$\text{deg}_{\text{eff}}(v) = \sum_{u \in N(v)} w(e_{vu}), \quad (8)$$

where $w(e_{vu})$ denotes the edge weight (often taken as the edge mass $m_1([v, u])$). This weighted degree quantifies how well-connected the vertex is to the graph structure, accounting for local density variations. Vertices with anomalously low effective degree relative to the global distribution may represent poorly sampled boundary regions where the discrete gradient flow is unreliable.

We convert both geometric measures to percentile ranks across all vertices: for d_k , we compute

$$p_k(v) = |\{u : d_k(u) \leq d_k(v)\}|/n,$$

which gives the fraction of vertices with hop- k distance at most that of v . Similarly, for effective degree, we compute

$$p_{\text{deg}}(v) = |\{u : \text{deg}_{\text{eff}}(u) \geq \text{deg}_{\text{eff}}(v)\}|/n,$$

giving the fraction of vertices with effective degree at least that of v (note the reversed inequality, as high degree indicates good connectivity). We retain extrema only if both geometric measures fall within acceptable ranges: typically $p_k(v) < 0.90$ and $p_{\text{deg}}(v) > 0.10$, though these thresholds may be adjusted based on the specific graph geometry and application requirements.

The complete refinement pipeline applies these stages sequentially: relative value filtering removes extrema with insufficient magnitude, overlap-based clustering and merging consolidates redundant features, and geometric filtering removes isolated or poorly-connected extrema. Each stage preserves the basin structure for retained extrema, so the final refined basin structure maintains complete information about gradient flow for all vertices assigned to surviving extrema. This multi-stage approach balances statistical and geometric considerations, ensuring that the final set of extrema represents genuine features of the estimated conditional expectation function rather than artifacts of discretization, sampling, or smoothing.

The filtering criteria involve several tunable parameters: the relative value thresholds ρ_{max} and ρ_{min} , the overlap threshold ω_{thld} , and the geometric percentile thresholds for p_k and p_{deg} . In practice, these parameters can be selected through exploratory analysis, examining how the number and prominence of retained extrema vary with parameter choices, or through cross-validation by assessing the stability of the resulting basin structure under perturbations of the smoothed function. Conservative choices (stricter thresholds) produce fewer extrema with higher confidence, while liberal choices preserve more potential features at the cost of retaining some spurious extrema. The modular design of the pipeline allows each filtering stage to be enabled or disabled independently, providing flexibility for different application contexts and data characteristics.

3.5 Basin Computation with Validated Gradient Flow

We turn now to the computational construction of basins of attraction using validated gradient flow. The basin structure provides the foundation for regional statistical inference, partitioning the sample space into regions where outcomes flow toward common extrema. Before developing the discrete algorithm, we recall the classical construction from smooth Morse theory, which both motivates our approach and highlights a fundamental difference between the continuous and discrete settings that has important implications for statistical applications.

Classical Basins and Gradient Flow Trajectories

In the smooth setting, consider a Morse function $f : M \rightarrow \mathbb{R}$ on a compact Riemannian manifold M without boundary. The gradient flow generates two types of trajectories from any regular point $x \in M$ (a point where $\nabla f(x) \neq 0$). The ascending trajectory satisfies the differential equation $\gamma'(t) = +\nabla f(\gamma(t))$ with initial condition $\gamma(0) = x$, following the direction of steepest increase until reaching a local maximum as $t \rightarrow \infty$. The descending trajectory satisfies $\gamma'(t) = -\nabla f(\gamma(t))$, flowing downhill to a local minimum. The Morse-Smale condition (generic transversality of stable and unstable manifolds) ensures that these trajectories are well-defined and unique for almost all starting points, with trajectories terminating at critical points rather than wandering indefinitely.

These trajectories induce maps $\pi_{\uparrow} : M \rightarrow \text{Max}(f)$ and $\pi_{\downarrow} : M \rightarrow \text{Min}(f)$ that assign to each point the terminus of its ascending and descending flows. For a local minimum m , the ascending basin (or unstable manifold) is defined as

$$A(m) = \{x \in M : \pi_{\downarrow}(x) = m\}, \quad (9)$$

containing all points whose descending flow terminates at m . For a local maximum M , the descending basin (or stable manifold) is

$$D(M) = \{x \in M : \pi_{\uparrow}(x) = M\}, \quad (10)$$

containing all points whose ascending flow terminates at M . The terminology reflects the direction of flow reaching the critical point: vertices in $A(m)$ descend to reach m , while vertices in $D(M)$ ascend to reach M .

A crucial property of the smooth setting is that basins of the same type are disjoint. No point can have descending flow terminating at two distinct minima, nor can ascending flow from a single point reach two distinct maxima. This uniqueness follows from the smooth dependence of gradient trajectories on initial conditions and the Morse-Smale transversality assumption. The ascending basins $\{A(m) : m \in \text{Min}(f)\}$ partition the manifold into disjoint regions, as do the descending basins $\{D(M) : M \in \text{Max}(f)\}$. The intersections $C(m, M) = A(m) \cap D(M)$ define gradient flow cells, which tile the manifold into regions where both ascending and descending flows have unique termini.

Non-Uniqueness in the Discrete Setting

When we discretize the gradient flow by restricting to a finite graph $G = (V, E)$, this uniqueness property fails. The discrete gradient flow is defined by following edges of steepest ascent or descent, but when multiple neighbors have identical or nearly identical function values, the choice of which edge to follow becomes ambiguous. More fundamentally, the graph topology itself creates situations where multiple distinct paths exist between a vertex and an extremum, each exhibiting monotonic function behavior, yet leading to different flow trajectories depending on the algorithmic tie-breaking rules.

Consider a simple example that illustrates this phenomenon. Let G be a star graph with a central vertex c and three arms, each consisting of a single edge connecting c to a terminal vertex. Label the terminal vertices v_1 , v_2 , and v_3 . Define a function \hat{y} with values $\hat{y}(v_1) = 0$,

$\hat{y}(v_2) = 0$, $\hat{y}(c) = 1$, and $\hat{y}(v_3) = 2$. The vertices v_1 and v_2 are both local minima (each has function value less than its only neighbor c), while v_3 is the unique local maximum.

Now consider the ascending basins. The vertex c has function value intermediate between the two minima and the maximum. From c , descending flow could reasonably proceed to either v_1 or v_2 , as both are neighbors with lower function values. If we break ties by choosing the neighbor with minimal function value, both v_1 and v_2 qualify equally. Different tie-breaking rules lead to different basin assignments: one rule might assign c to $A(v_1)$, another to $A(v_2)$. Regardless of the choice, the resulting ascending basins are not disjoint. If $c \in A(v_1)$, then since v_2 is a minimum, we have $A(v_2) = \{v_2\}$. But if we run the basin construction algorithm symmetrically from both minima using breadth-first exploration (as we describe below), the vertex c appears reachable from both v_1 and v_2 through monotone descending paths ($v_1 \rightarrow c$ and $v_2 \rightarrow c$ both ascend, so tracing backward from c can descend to either minimum). Thus c potentially belongs to both ascending basins, creating an intersection $A(v_1) \cap A(v_2) \ni c$.

This non-uniqueness has important statistical implications. In the continuous setting, the partition into gradient flow cells provides an unambiguous spatial decomposition for regional inference. In the discrete setting, ambiguous vertices near basin boundaries require explicit resolution through tie-breaking rules or probabilistic assignment. Our algorithm addresses this by using breadth-first exploration to establish basin membership definitively based on discovery order, but we acknowledge that alternative algorithmic choices could produce different basin structures for ambiguous vertices. This sensitivity to algorithmic details suggests that statistical inference should focus on vertices deep within basins, where flow direction is unambiguous, rather than on vertices near boundaries where multiple extrema exert comparable influence.

Backward Tracing Through Breadth-First Exploration

We construct basins through breadth-first exploration that works backward along flow trajectories. The key insight is that to find all vertices whose ascending flow reaches a maximum M , we start at M itself and explore outward, accepting vertices that lie "below" already-accepted vertices in function value. This backward tracing ensures that every accepted vertex has a monotone increasing path to M , which corresponds precisely to the forward ascending trajectory from that vertex terminating at M .

Consider the descending basin $D(M) = \{v : \pi_{\uparrow}(v) = M\}$ of a local maximum M . We initialize the basin with $D(M) = \{M\}$ and a queue containing M . We maintain a distance map $\text{dist}[v]$ recording the hop distance from M to each accepted vertex, and a predecessor map $\text{pred}[v]$ tracking the path back to M . The algorithm proceeds iteratively: while the queue is non-empty, we dequeue a vertex $u \in D(M)$ and examine each neighbor $v \notin D(M)$. If $\hat{y}(v) < \hat{y}(u)$, then the edge $[v, u]$ represents a valid step in an ascending trajectory from v toward M (since moving from v to u increases the function value). To verify that this edge participates in genuine gradient flow rather than an artifactual jump across basins, we apply the validation criterion from Section 3.3.

For edges with length $\Delta_{uv} \leq \tau_q$ (below the quantile threshold), we accept v immediately, as short edges are presumed to follow local manifold geometry faithfully. For long edges

with $\Delta_{uv} > \tau_q$, we compute the shortest alternative path $\gamma_{[u,v]}$ from u to v in the graph $G \setminus \{[u,v]\}$ (temporarily removing the direct edge). If no such path exists, the edge is essential for connectivity and we accept it by default. If an alternative path exists, we evaluate its co-monotonicity coefficient $\text{cm}(\hat{y}; \gamma_{[u,v]})$. For descending exploration (where we seek vertices with $\hat{y}(v) < \hat{y}(u)$ that can ascend to M), the path from u to v should exhibit descending monotonicity (function values decreasing along the path from u toward v). We require $\text{cm}(\hat{y}; \gamma_{[u,v]}) \leq -\theta$ for a threshold $\theta \in [0.85, 1.0]$. If this condition holds, the long edge is validated and we accept v into the basin, setting $\text{dist}[v] = \text{dist}[u] + 1$, $\text{pred}[v] = u$, and adding v to the queue for further exploration. If validation fails, we reject this particular edge from u to v and continue examining other neighbors.

This backward exploration guarantees that every vertex in $D(M)$ is connected to M through a validated path where function values increase monotonically. Vertices reachable from M only through invalidated long edges remain outside the basin, preventing spurious basin jumping while maintaining computational efficiency. The validation occurs lazily during breadth-first search, so we evaluate co-monotonicity only for long edges that actually arise in potential basin membership, avoiding exhaustive validation of the entire graph.

Ascending basins for local minima follow the same algorithmic structure with reversed monotonicity conditions. To construct $A(m) = \{v : \pi_{\downarrow}(v) = m\}$ for a local minimum m , we initialize with $A(m) = \{m\}$ and perform breadth-first exploration accepting neighbors v of vertices $u \in A(m)$ when $\hat{y}(v) > \hat{y}(u)$. This explores upward from m (in the ascending direction) while tracing descending flow trajectories backward, identifying all vertices from which descending flow reaches m . For long edges, we require $\text{cm}(\hat{y}; \gamma_{[u,v]}) \geq \theta$, validating that the alternative path from u to v exhibits ascending monotonicity consistent with the upward exploration direction.

The complete partition of vertices into basins emerges from running this algorithm for all detected local extrema. Due to the non-uniqueness discussed above, some vertices may be discovered during exploration from multiple extrema of the same type. We resolve such conflicts through tie-breaking rules based on discovery order: the first extremum to reach a vertex during breadth-first exploration claims that vertex for its basin. This deterministic rule ensures each vertex belongs to exactly one ascending basin and exactly one descending basin, though the specific assignment depends on the order in which extrema are processed. Alternative tie-breaking strategies include assigning ambiguous vertices based on minimal path length to extrema, maximal function value difference along paths, or probabilistic assignment proportional to path validation scores. The sensitivity of boundary vertex assignments to these algorithmic choices reinforces that robust inference should focus on the interior of basins rather than their boundaries.

For vertices that remain unassigned after processing all extrema, we have two options. The first is to leave them as isolated singletons, which may occur for vertices in flat regions where no clear gradient direction exists. The second is to perform a final assignment phase where unassigned vertices are allocated to the nearest basin based on graph distance, function value similarity, or other proximity measures. In practice, validated gradient flow with appropriate quantile and monotonicity thresholds produces nearly complete basin coverage, with unassigned vertices arising primarily in highly ambiguous flat regions or poorly connected boundary zones.

Algorithm 1 Validated Descending Basin Computation

Input: Graph $G = (V, E)$, function $\hat{y} : V \rightarrow \mathbb{R}$, local maximum M , quantile threshold q , monotonicity threshold θ

Output: Descending basin $D(M) = \{v : \pi_{\uparrow}(v) = M\} \subseteq V$

Compute edge length quantile $\tau_q \leftarrow \text{quantile}(\{\Delta_e : e \in E\}, q)$

Initialize $D(M) \leftarrow \{M\}$, queue $\leftarrow [M]$, dist[M] $\leftarrow 0$, pred[M] $\leftarrow \text{null}$

while queue is not empty **do**

$u \leftarrow \text{dequeue}()$

for each neighbor v of u in G **do**

if $v \notin D(M)$ **and** $\hat{y}(v) < \hat{y}(u)$ **then**

$e \leftarrow [u, v]$

if $\Delta_e \leq \tau_q$ **then**

 valid $\leftarrow \text{true}$ {Short edge: v can ascend through u to M }

else

$\gamma_{[u,v]} \leftarrow \text{ShortestPath}(u, v, G \setminus \{e\})$

if $\gamma_{[u,v]} = \emptyset$ **then**

 valid $\leftarrow \text{true}$ {Edge essential for connectivity}

else

 valid $\leftarrow (\text{cm}(\hat{y}; \gamma_{[u,v]}) \leq -\theta)$ {Validate descending path monotonicity}

end if

end if

if valid **then**

$D(M) \leftarrow D(M) \cup \{v\}$

 dist[v] $\leftarrow \text{dist}[u] + 1$

 pred[v] $\leftarrow u$

 enqueue(v)

end if

end if

end for

end while

return $D(M)$, dist, pred

Computational Complexity and Practical Considerations

The algorithm’s computational cost decomposes into several components. The initial quantile computation requires sorting all edge lengths, an $O(|E| \log |E|)$ operation performed once before basin construction begins. For each extremum, the breadth-first exploration visits each vertex at most once and examines each incident edge at most once, giving $O(|V| + |E|)$ per extremum in the absence of validation. When validation is required for a long edge $e = [u, v]$, computing the shortest alternative path using breadth-first search costs $O(|E|)$ in sparse graphs. Evaluating the co-monotonicity coefficient along a path of length ℓ costs $O(\ell)$, typically $O(\log |V|)$ for paths in graphs with good expansion properties.

The total validation cost depends on the quantile threshold q and the graph geometry. Choosing $q \in [0.75, 0.90]$ ensures that only the longest 10-25% of edges require validation. In well-structured graphs where long edges are rare and localized, validation overhead remains modest. In pathological cases where many long edges connect distant regions, validation costs can approach $O(L \cdot |E|)$ where L is the number of long edges examined during all basin explorations. For typical applications with $n = 500$ -5000 vertices and $k = 10$ -50 nearest neighbors, basin computation completes in seconds to minutes on modern hardware, with validation adding at most a factor of 2-5 overhead compared to naive gradient flow.

Memory requirements are dominated by storing the graph structure ($O(|E|)$ for adjacency lists and edge lengths), the distance and predecessor maps for each basin ($O(|V|)$ per extremum), and temporary storage for shortest path computations ($O(|V|)$). For graphs with $n = 10^4$ vertices and moderate degree, total memory consumption remains well under 1 GB, enabling in-memory computation on standard workstations. Parallel computation across extrema is straightforward, as basin constructions are independent until the final tie-breaking phase, offering near-linear speedup on multi-core systems.

4. Co-Monotonicity Coefficients

Having established gradient flow partitions through local extrema gradient flow basins, we turn to quantifying associations between functions on graph vertices. The fundamental question driving this development is: how should we measure whether two functions vary together or oppositely along the edges of a graph? Classical correlation coefficients treat all observations as equally related, ignoring the geometric structure encoded by the graph. We seek measures that respect this structure, detecting directional concordance locally while adapting to spatial heterogeneity in association patterns.

4.1 Global Association Measures

Consider an outcome function $y : V \rightarrow \mathbb{R}$ and a potential predictor $z : V \rightarrow \mathbb{R}$ defined on the vertices of a graph $G = (V, E)$ derived from high-dimensional data. Standard correlation analysis computes the Pearson coefficient

$$\rho(y, z) = \frac{\text{Cov}(y, z)}{\sigma_y \sigma_z} = \frac{\sum_{v \in V} (y(v) - \bar{y})(z(v) - \bar{z})}{\sqrt{\sum_{v \in V} (y(v) - \bar{y})^2} \sqrt{\sum_{v \in V} (z(v) - \bar{z})^2}}, \quad (11)$$

where \bar{y} and \bar{z} denote sample means. This measure treats all vertex pairs equally, implicitly assuming that observations at vertices v and u are as related as observations at v and w , regardless of whether edges connect these pairs in the graph. When the graph encodes meaningful proximity relationships, as in spatial data or network analysis, this assumption discards valuable structural information. In particular, when a feature z varies concordantly with y in one region of the graph but discordantly in another, these opposing local relationships may cancel in the global correlation, yielding a coefficient near zero despite strong region-specific associations.

Moreover, correlation measures linear association in terms of deviations from means, which may not align with the geometric properties of interest. Within a gradient flow cell where the outcome y varies monotonically, we seek features that exhibit monotone co-variation along the same paths, increasing when y increases and decreasing when y decreases. Mutual information addresses nonlinearity and can be computed on graph structures, providing a viable alternative for quantifying associations between vertex functions. However, mutual information and other global measures produce a single summary of the relationship between y and z across all vertices. They cannot reveal spatial heterogeneity in association patterns, nor can they identify regions where the relationship is strong versus weak, or positive versus negative. When association structure varies across the graph, as commonly occurs in gradient flow cells with different monotonic behaviors, a single global measure obscures this regional variation. While mutual information can in principle be localized to vertices or paths through kernel-weighted density estimation (see Appendix B), such approaches introduce substantial practical challenges in estimation and interpretation.

Co-monotonicity coefficients address this limitation by providing vertex-level measures rather than global summaries. For each vertex v , we compute a coefficient $c(y, z; v)$ that quantifies directional concordance between y and z within the local neighborhood of v . This yields a function $c : V \rightarrow [-1, 1]$ that maps vertices to association strengths, enabling identification of regions where features exhibit strong positive co-variation, regions with negative relationships, and regions where associations are weak or absent. The coefficients have intuitive geometric interpretation: they measure whether y and z tend to increase or decrease together across edges incident to each vertex, directly capturing the directional concordance that characterizes monotonic co-variation within gradient flow structures. This vertex-level resolution proves essential for regional inference, where statistical power comes from identifying coherent association patterns within cells while allowing relationships to differ across cells.

We formalize these concepts through two complementary perspectives on directional concordance. At each vertex $v \in V$, we define a coefficient $c(y, z; v) \in [-1, 1]$ that measures whether y and z tend to increase or decrease together across edges incident to v . This local measure naturally extends to paths $\gamma = (\gamma_0, \gamma_1, \dots, \gamma_n)$, where we compute $c(y, z; \gamma)$ to quantify directional concordance along the sequence of edges comprising γ . The vertex-based coefficients enable spatial mapping of association patterns, while path-based coefficients characterize monotonic behavior along gradient flow trajectories. We develop both perspectives in the following sections, beginning with the vertex-centered formulation.

4.2 Vertex-Level Co-Monotonicity Coefficients

We seek vertex-level measures that quantify whether two functions increase or decrease together across edges in local neighborhoods. The approach builds on edge-wise directional concordance, aggregating signed products of function changes across incident edges with appropriate normalization to yield coefficients bounded in $[-1, 1]$.

We begin by formalizing the notion of directional agreement along a single edge. Let $e = [v, u] \in E$ be an edge connecting vertices v and u , and define the edge difference operator acting on a function $f : V \rightarrow \mathbb{R}$ by

$$\Delta_e f = f(u) - f(v). \quad (12)$$

This operator measures the change in f when moving from v to u along edge e . The choice of orientation (which vertex to designate as initial point) is arbitrary; what matters is that we consistently use the same orientation for all functions when computing products of differences, ensuring that the product captures directional concordance rather than being affected by orientation choices.

The product $\Delta_e y \cdot \Delta_e z$ captures the directional concordance of y and z along edge e . When both functions increase ($\Delta_e y > 0$ and $\Delta_e z > 0$) or both decrease ($\Delta_e y < 0$ and $\Delta_e z < 0$), the product is positive, indicating co-monotonic behavior. When the functions change in opposite directions, the product is negative, indicating anti-monotonic behavior. When at least one function remains constant across the edge, the product vanishes.

To construct a vertex-level measure, we aggregate these products over edges incident to each vertex. Let $N(v)$ denote the set of neighbors of v (vertices connected to v by edges). A natural approach sums the weighted products $w_e \Delta_e y \cdot \Delta_e z$ over all edges $e = [v, u]$ with $u \in N(v)$, where $w_e \geq 0$ are edge weights. However, this raw sum depends on the scales of y and z , making comparisons across different function pairs problematic. We address this by normalizing in a manner analogous to Pearson correlation, dividing by the geometric mean of the total weighted squared changes in each function separately. This normalization ensures the resulting coefficient lies in $[-1, 1]$ regardless of function scales, with extremal values indicating perfect proportional co-variation or anti-variation.

Given functions $y, z : V \rightarrow \mathbb{R}$ on a weighted graph $G = (V, E)$ with edge weights $w_e \geq 0$, the correlation-type co-monotonicity coefficient at vertex v is

$$\text{cm}_{\text{cor}}(y, z; w)(v) = \frac{\sum_{u \in N(v)} w_e \Delta_e y \cdot \Delta_e z}{\sqrt{\sum_{u \in N(v)} w_e (\Delta_e y)^2} \sqrt{\sum_{u \in N(v)} w_e (\Delta_e z)^2}}, \quad (13)$$

where $e = [v, u]$ denotes the edge connecting v and u , and $\Delta_e y = y(u) - y(v)$, $\Delta_e z = z(u) - z(v)$ are the edge differences oriented away from v . When either denominator term vanishes (indicating that one of the functions is constant across all edges incident to v), we define $\text{cm}_{\text{cor}}(y, z; w)(v) = 0$ by convention.

The normalization by geometric mean of squared changes ensures that $\text{cm}_{\text{cor}}(y, z; w)(v) \in [-1, 1]$ for all vertices, with extremal values achieved under perfect proportionality. If $\Delta_e z = k \Delta_e y$ for some constant $k > 0$ across all edges incident to v , then $\text{cm}_{\text{cor}}(y, z; w)(v) = 1$.

If $\Delta_e z = -k\Delta_e y$ for $k > 0$, then $\text{cm}_{\text{cor}}(y, z; w)(v) = -1$. The coefficient vanishes when positive and negative products balance in a squared-magnitude-weighted sense.

A particularly important special case arises when edge weights are chosen as $w_e = 1/\ell_e$ where ℓ_e denotes the length of edge e . This derivative-weighted co-monotonicity coefficient takes the form

$$\text{cm}_{\text{cor},\partial}(y, z)(v) = \frac{\sum_{u \in N(v)} \frac{\Delta_e y}{\ell_e} \cdot \frac{\Delta_e z}{\ell_e}}{\sqrt{\sum_{u \in N(v)} \left(\frac{\Delta_e y}{\ell_e}\right)^2} \sqrt{\sum_{u \in N(v)} \left(\frac{\Delta_e z}{\ell_e}\right)^2}}, \quad (14)$$

where the ratios $\Delta_e y/\ell_e$ and $\Delta_e z/\ell_e$ approximate directional derivatives of y and z along the edges. This form admits a compelling geometric interpretation: on a smooth Riemannian manifold, the coefficient measures the cosine of the angle between gradient vector fields, providing theoretical justification for this normalization choice. We develop this connection formally in Section 4.4, where we show that $\text{cm}_{\text{cor},\partial}$ arises naturally from the Riemannian metric structure on smooth manifolds.

Throughout the remainder of this paper, we adopt the simplified notation $\text{cm}(y, z; w)(v)$ to denote the correlation-type co-monotonicity coefficient $\text{cm}_{\text{cor}}(y, z; w)(v)$ when the normalization scheme is clear from context. For derivative weighting, we write $\text{cm}_\partial(y, z)(v)$ as shorthand for $\text{cm}_{\text{cor},\partial}(y, z)(v)$. The subscript "cor" is retained only when explicitly contrasting with alternative normalizations.

4.3 Geometric Interpretation via Gradient Alignment

We now establish a rigorous connection between correlation-type co-monotonicity and angular correlation of gradients on smooth Riemannian manifolds. This provides both theoretical justification for the derivative-weighted formulation and intuitive geometric meaning for the coefficient values.

Suppose data $X = \{x_1, \dots, x_n\}$ are sampled from a smooth d -dimensional Riemannian manifold M embedded in \mathbb{R}^D for $D \geq d$. Let $y, z : M \rightarrow \mathbb{R}$ be smooth functions with non-vanishing gradients in a neighborhood of a point $x_v \in M$. The k -nearest neighbor graph G_n constructed from X approximates M in the limit of dense sampling, with appropriate scaling $k = k(n)$ such that $k/n \rightarrow 0$ and $k/\log n \rightarrow \infty$ as $n \rightarrow \infty$.

For a vertex v corresponding to point $x_v \in M$, the neighborhood $N(v)$ consists of the k nearest sample points, which are approximately uniformly distributed in a geodesic ball $B_{r_k}(x_v)$ of radius r_k around x_v , where r_k is the distance to the k -th nearest neighbor. As $n \rightarrow \infty$, we have $r_k \rightarrow 0$ with rate determined by the local density of the sampling distribution and the scaling of k .

Consider an edge $e = [v, u]$ connecting v to a neighbor u at point $x_u \in M$ with $d_M(x_v, x_u) = \Delta_e$, where d_M denotes the Riemannian distance on M . For small Δ_e , the function difference can be approximated by the directional derivative:

$$\Delta_e y = y(x_u) - y(x_v) = \langle \nabla_M y(x_v), \xi_e \rangle \Delta_e + O(\Delta_e^2), \quad (15)$$

where $\xi_e \in T_{x_v}M$ is the unit tangent vector at x_v pointing in the direction of the geodesic from x_v to x_u , and $\nabla_M y$ denotes the Riemannian gradient of y on M . Dividing by edge length gives

$$\frac{\Delta_e y}{\Delta_e} = \langle \nabla_M y(x_v), \xi_e \rangle + O(\Delta_e). \quad (16)$$

Similarly, for the second function,

$$\frac{\Delta_e z}{\Delta_e} = \langle \nabla_M z(x_v), \xi_e \rangle + O(\Delta_e). \quad (17)$$

The numerator of $\text{cm}_{\text{cor},\partial}(y, z)(v)$ aggregates products of these discrete directional derivatives over the neighborhood $N(v)$. As $n \rightarrow \infty$ and the neighborhood becomes dense, this sum approximates a Riemann integral over directions. Specifically, for uniformly distributed neighbors in a geodesic ball, the directions $\{\xi_e : u \in N(v)\}$ become equidistributed on the unit sphere $S^{d-1} \subset T_{x_v}M$ in the tangent space. We obtain

$$\sum_{u \in N(v)} \frac{\Delta_e y}{\Delta_e} \cdot \frac{\Delta_e z}{\Delta_e} \approx \sum_{u \in N(v)} \langle \nabla_M y(x_v), \xi_e \rangle \langle \nabla_M z(x_v), \xi_e \rangle \quad (18)$$

$$\rightarrow |N(v)| \int_{S^{d-1}} \langle \nabla_M y(x_v), \xi \rangle \langle \nabla_M z(x_v), \xi \rangle d\sigma(\xi), \quad (19)$$

where $d\sigma$ denotes the uniform probability measure on the unit sphere S^{d-1} .

We evaluate this integral using a standard result from directional statistics. For any two vectors $\mathbf{a}, \mathbf{b} \in \mathbb{R}^d$, the integral of their directional projections squared over the unit sphere satisfies

$$\int_{S^{d-1}} \langle \mathbf{a}, \xi \rangle \langle \mathbf{b}, \xi \rangle d\sigma(\xi) = \frac{1}{d} \langle \mathbf{a}, \mathbf{b} \rangle. \quad (20)$$

This identity follows from expanding the inner products in coordinates and using the fact that for $i \neq j$, we have $\int_{S^{d-1}} \xi_i \xi_j d\sigma(\xi) = 0$ by symmetry, while $\int_{S^{d-1}} \xi_i^2 d\sigma(\xi) = 1/d$ by normalization (since $\sum_{i=1}^d \int_{S^{d-1}} \xi_i^2 d\sigma(\xi) = \int_{S^{d-1}} |\xi|^2 d\sigma(\xi) = 1$ and all d components contribute equally). Applying this to $\mathbf{a} = \nabla_M y(x_v)$ and $\mathbf{b} = \nabla_M z(x_v)$, we obtain

$$\sum_{u \in N(v)} \frac{\Delta_e y}{\Delta_e} \cdot \frac{\Delta_e z}{\Delta_e} \rightarrow \frac{|N(v)|}{d} \langle \nabla_M y(x_v), \nabla_M z(x_v) \rangle. \quad (21)$$

The denominator terms undergo similar approximation. We have

$$\sum_{u \in N(v)} \left(\frac{\Delta_e y}{\Delta_e} \right)^2 \approx \sum_{u \in N(v)} \langle \nabla_M y(x_v), \xi_e \rangle^2 \quad (22)$$

$$\rightarrow |N(v)| \int_{S^{d-1}} \langle \nabla_M y(x_v), \xi \rangle^2 d\sigma(\xi) \quad (23)$$

$$= \frac{|N(v)|}{d} |\nabla_M y(x_v)|^2, \quad (24)$$

where the final equality again uses the directional integral formula with $\mathbf{a} = \mathbf{b} = \nabla_M y(x_v)$. Similarly,

$$\sum_{u \in N(v)} \left(\frac{\Delta_e z}{\Delta_e} \right)^2 \rightarrow \frac{|N(v)|}{d} |\nabla_M z(x_v)|^2. \quad (25)$$

Combining these results, we obtain the limiting formula:

$$\lim_{n \rightarrow \infty} \text{cm}_{\text{cor}, \partial}(y, z)(v) = \frac{\frac{|N(v)|}{d} \langle \nabla_M y(x_v), \nabla_M z(x_v) \rangle}{\sqrt{\frac{|N(v)|}{d} |\nabla_M y(x_v)|^2} \sqrt{\frac{|N(v)|}{d} |\nabla_M z(x_v)|^2}} \quad (26)$$

$$= \frac{\langle \nabla_M y(x_v), \nabla_M z(x_v) \rangle}{|\nabla_M y(x_v)| \cdot |\nabla_M z(x_v)|} \quad (27)$$

$$= \cos \theta(x_v), \quad (28)$$

where $\theta(x_v) \in [0, \pi]$ denotes the angle between the gradient vectors $\nabla_M y(x_v)$ and $\nabla_M z(x_v)$ in the tangent space $T_{x_v} M$.

This limiting interpretation provides compelling geometric meaning for the correlation-type co-monotonicity coefficient. When $\text{cm}_{\text{cor}, \partial}(y, z)(v) \approx 1$, the gradients of y and z are nearly parallel at the corresponding point in M , indicating that both functions increase in approximately the same direction. When $\text{cm}_{\text{cor}, \partial}(y, z)(v) \approx -1$, the gradients are anti-parallel, so the functions increase in opposite directions. When $\text{cm}_{\text{cor}, \partial}(y, z)(v) \approx 0$, the gradients are approximately orthogonal, indicating that the functions vary independently in different tangent directions.

This geometric perspective explains why derivative weighting is natural for smooth functions on manifolds: it captures intrinsic geometric association that is independent of the ambient coordinate system used to represent the data. The normalization by edge length converts raw differences into discrete approximations of directional derivatives, which are the natural geometric quantities for characterizing function variation on Riemannian manifolds.

In finite samples with discrete neighborhoods, this limiting result suggests why the correlation-type formulation performs well in practice. The asymptotic formula assumes the neighborhood becomes dense in the tangent space, providing approximately uniform directional coverage. With finite k , the discrete neighborhood necessarily undersamples certain tangent directions, but the correlation-type normalization remains stable provided both functions exhibit sufficient variation across incident edges. The geometric mean in the denominator ensures the coefficient scales appropriately even when gradient magnitudes vary spatially, making the measure robust to heterogeneous signal patterns common in high-dimensional biological data.

4.4 Edge Weighting Schemes

The correlation-type co-monotonicity coefficient defined in Section 4.2 allows flexible edge weighting through the parameters $w_e \geq 0$. The choice of weights determines which aspects of directional concordance the measure emphasizes, with different schemes appropriate

for different data structures and inferential goals. We examine three canonical weighting schemes that arise naturally in geometric data analysis.

The simplest choice assigns uniform weight to all edges: $w_e = 1$ for all $e \in E$. This unit weighting scheme treats edges equally regardless of their length, emphasizing the combinatorial structure of the graph. The resulting coefficient

$$\text{cm}_{\text{cor}}(y, z; 1)(v) = \frac{\sum_{u \in N(v)} \Delta_e y \cdot \Delta_e z}{\sqrt{\sum_{u \in N(v)} (\Delta_e y)^2} \sqrt{\sum_{u \in N(v)} (\Delta_e z)^2}} \quad (29)$$

directly correlates the raw function differences across edges without geometric normalization. Unit weighting is appropriate when edge lengths are roughly comparable, as in regular lattices or uniformly sampled grids, or when the graph represents abstract relationships rather than geometric proximity. For graphs constructed from irregular spatial samples where edge lengths vary substantially, unit weighting may overweight contributions from long edges that span large distances in the underlying space, obscuring local patterns of directional concordance.

To account for geometric scaling, we employ derivative weighting as introduced in Section 4.2. Setting $w_e = 1/\ell_e$ where ℓ_e denotes edge length yields

$$\text{cm}_{\text{cor},\partial}(y, z)(v) = \frac{\sum_{u \in N(v)} \frac{\Delta_e y}{\ell_e} \cdot \frac{\Delta_e z}{\ell_e}}{\sqrt{\sum_{u \in N(v)} \left(\frac{\Delta_e y}{\ell_e}\right)^2} \sqrt{\sum_{u \in N(v)} \left(\frac{\Delta_e z}{\ell_e}\right)^2}}, \quad (30)$$

which correlates discrete directional derivatives rather than raw differences. This normalization by edge length has two beneficial effects. First, it prevents long edges from dominating the coefficient: a large absolute change $\Delta_e y$ across a long edge ℓ_e corresponds to a moderate derivative $\Delta_e y/\ell_e$, giving it appropriate weight relative to shorter edges. Second, as established in Section 4.3, derivative weighting ensures that the coefficient approximates the cosine of the angle between gradient vectors on smooth manifolds, providing intrinsic geometric meaning independent of coordinate representation. Derivative weighting is appropriate when functions represent continuous quantities sampled at irregular positions and we wish to assess co-variation in the underlying continuous fields rather than artifacts of the sampling pattern.

A third weighting scheme arises naturally from spectral graph theory and diffusion processes on graphs. In the graph Laplacian framework, edge weights often represent conductances c_e that govern the rate of diffusion between adjacent vertices. Using $w_e = c_e$ yields a coefficient that emphasizes edges with high conductance, reflecting the effective connectivity structure rather than purely geometric proximity. For graphs derived from kernel-weighted similarity matrices where $c_e = \exp(-d_e^2/\sigma^2)$ with d_e denoting distance and σ controlling bandwidth, conductance weighting downweights distant connections while preserving strong local relationships. This scheme proves useful when the graph encodes probabilistic or functional relationships rather than strict geometric structure, as in biological networks where interaction strength varies independently of physical distance.

The choice among these weighting schemes depends on the data structure and the inferential question. Derivative weighting is generally preferred for spatially embedded data

where geometric scaling matters and functions are approximately continuous. Unit weighting suffices for combinatorial graphs or when edge lengths are comparable. Conductance weighting addresses situations where edge importance varies beyond geometric considerations, capturing the effective strength of relationships encoded by the graph structure. In all cases, the correlation-type normalization ensures coefficients remain bounded in $[-1, 1]$ and retain interpretability as measures of directional concordance scaled by the geometric mean of function variations.

4.5 Scale Artifacts and Geometric Smoothing

The unit and derivative weighting schemes measure directional concordance at different geometric scales, which can produce substantial discrepancies when graph edge lengths vary heterogeneously. We demonstrate this phenomenon through an empirical analysis of spontaneous preterm birth associations in vaginal microbiome data (Figure 4), then introduce geometric smoothing as a principled approach for scale-consistent inference.

Consider a k -nearest neighbor graph constructed from compositional data, where edge lengths ℓ_e represent distances between samples in a high-dimensional feature space. The distribution of edge lengths typically exhibits considerable heterogeneity: most edges connect samples at moderate distances (say, $0.05 < \ell_e < 0.15$), but some edges span very short distances ($\ell_e < 0.01$) between nearly identical samples arising from repeated measurements, high sampling density in certain regions, or genuine biological clustering. Under derivative weighting with $w_e = 1/\ell_e$, these very short edges receive extreme weights that can exceed typical edge weights by factors of 10^3 to 10^5 .

We assessed the practical impact of scale heterogeneity by computing both unit-weighted and derivative-weighted correlation coefficients between sPTB prevalence and 106 phylotype abundances across 2,117 vertices in a vaginal microbiome graph, yielding 224,202 vertex-phylotype pairs. Figure 4A displays the relationship between these two measures for all pairs. While most pairs cluster near the diagonal, indicating agreement between weighting schemes, substantial discrepancies appear at 964 pairs (0.43% of total, highlighted in red) where $|\text{cm}_{\text{cor}}(y, z; 1)(v) - \text{cm}_{\text{cor},\delta}(y, z)(v)| > 0.75$. The scatter reveals that unit and derivative weighting can yield markedly different assessments of the same biological association. One extreme case displayed opposite signs: unit weighting yielded -0.618 while derivative weighting yielded $+0.906$ for the association between sPTB and *Corynebacterium imitans* at a specific vertex.

Detailed examination of this extreme case revealed the mechanism underlying such discrepancies. The vertex had 37 neighbors, but five edges with lengths below 0.005 received derivative weights exceeding 200-fold typical values, dominating the calculation and yielding opposite-sign concordance from the broader neighborhood pattern. The unit-weighted coefficient averaged uniformly across all 37 edges, yielding a negative association reflecting the majority pattern. The derivative-weighted coefficient was driven almost entirely by the five extremely short edges, which exhibited positive concordance while the remaining 32 edges showed negative concordance.

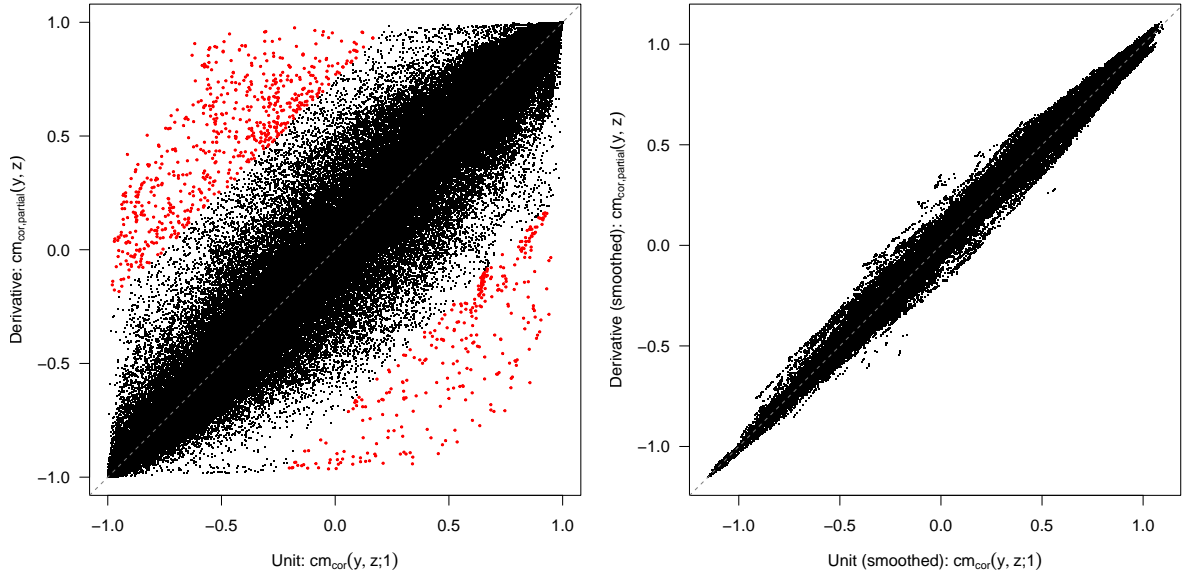


Figure 4: Scale artifacts in co-monotonicity coefficients are eliminated by geometric smoothing. (A) Raw correlation-type coefficients computed with derivative versus unit weighting for sPTB prevalence and 106 phylotypes across 224,402 vertex-phylotype pairs. Red points indicate pairs with large discrepancies ($|\text{difference}| > 0.75$). (B) The same coefficients after geometric smoothing via graph Laplacian filtering. Smoothing eliminates scale-dependent discrepancies, demonstrating that both weighting schemes recover nearly identical association structure at consistent geometric scale.

This behavior reflects fundamentally different notions of local association. Unit weighting measures concordance across the combinatorial neighborhood, treating all connected vertices equally regardless of their geometric separation. Derivative weighting measures concordance in the geometric tangent space, where very short edges approximate infinitesimal neighborhoods and receive proportionally large weight according to the distance gradient. When micro-scale patterns at edges shorter than 0.01 differ from meso-scale patterns at edges between 0.05 and 0.15, the two measures capture genuinely distinct geometric phenomena operating at different scales. The derivative-weighted coefficient becomes sensitive to association structure at arbitrarily fine scales determined by the shortest edges in the graph, which may reflect sampling artifacts rather than meaningful biological variation. Conversely, the unit-weighted coefficient treats all scales equally within the combinatorial neighborhood, potentially obscuring geometric structure encoded in edge lengths. Without additional constraints, neither measure uniquely captures the associations of scientific interest.

These findings demonstrate that raw co-monotonicity coefficients exhibit scale-dependent artifacts that obscure biological signal. We address this scale heterogeneity through geometric smoothing of the computed coefficient matrices. The graph Laplacian low-pass filter employed for smoothing response functions (Section 3) naturally extends to smoothing association maps. For a co-monotonicity matrix $\text{CM}(y, Z)$ with dimensions $n \times m$, we apply the smoothing operation to each column independently:

$$\text{CM}_{\text{smooth}}(y, Z) = [\text{smooth}(\text{CM}(y, Z)[:, j])]_{j=1, \dots, m}, \quad (31)$$

where the smoothing uses the same regularization parameter λ selected for the response y via generalized cross-validation or similar criteria. This ensures that associations are analyzed at the same geometric scale as the response variation itself, maintaining consistency throughout the analysis pipeline.

Figure 4B displays the result of applying this smoothing procedure to both unit-weighted and derivative-weighted coefficients. The effect is substantial: the mean absolute difference between the two measures drops from 0.089 to 0.029, the 95th percentile decreases from 0.329 to 0.095, and all 964 pairs with raw differences exceeding 0.75 reduce to disagreements below this threshold after smoothing. The smoothed coefficients align almost perfectly along the diagonal, with correlation exceeding 0.999 between the two measures. The extreme case of opposite signs resolved to agreement: both smoothed coefficients yielded +0.82, confirming a positive association at the biologically relevant scale while filtering out the micro-scale artifact from very short edges. This near-perfect concordance after smoothing demonstrates that unit and derivative weighting recover the same underlying association structure once analyzed at a consistent geometric scale.

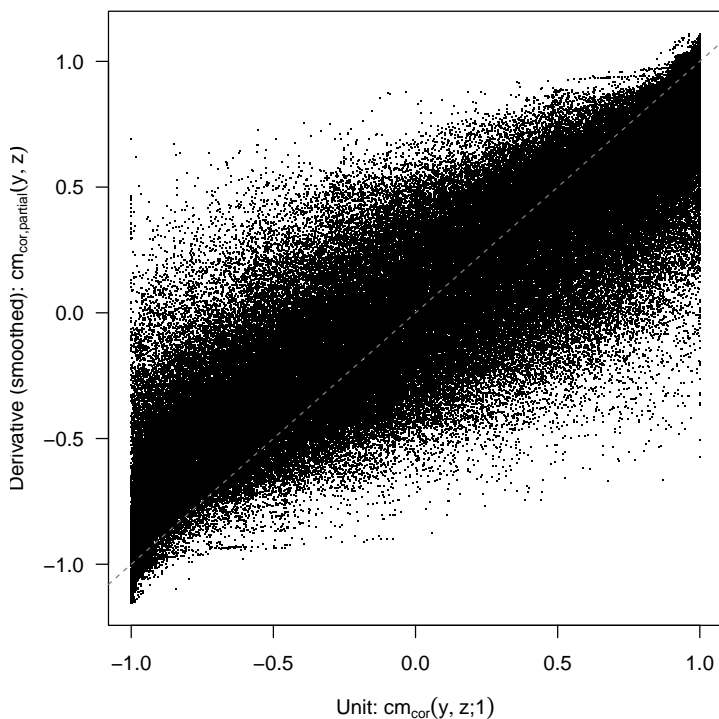


Figure 5: Raw unit-weighted coefficients do not match smoothed derivative-weighted coefficients, demonstrating that smoothing fundamentally transforms both weighting schemes. Comparison of raw unit-weighted co-monotonicity coefficients versus smoothed derivative-weighted coefficients for sPTB prevalence and 106 phylotypes across 224,402 vertex-phylo-type pairs. The wide scatter (Gini mean difference: 0.322) contrasts with the tight agreement between smoothed unit-weighted and smoothed derivative-weighted coefficients (Figure 4B), confirming that geometric smoothing modifies association structure rather than merely adjusting one scheme to match the other.

Importantly, both unit-weighted and derivative-weighted coefficients are substantially mod-

ified by the smoothing process. Figure 5 compares raw unit-weighted coefficients with smoothed derivative-weighted coefficients, revealing persistent discrepancies throughout the distribution. While the mean difference is near zero (-0.007), substantial scatter remains with the 5th and 95th percentiles at -0.490 and 0.453 respectively, range from -1.69 to 1.57 , and Gini mean difference of 0.322 . This wide scatter contrasts sharply with the tight agreement between smoothed unit-weighted and smoothed derivative-weighted coefficients (Figure 4B), confirming that geometric smoothing substantively modifies the association structure for both weighting schemes rather than simply adjusting one to match the raw values of the other.

This empirical validation reveals that the apparent conflict between unit and derivative weighting reflects scale artifacts rather than fundamental methodological differences. The biologically meaningful associations exist at the geometric scale determined by the graph Laplacian regularization, which balances signal fidelity against noise suppression. Micro-scale variations captured by extreme derivative weights on very short edges represent either sampling artifacts such as repeated measurements and density fluctuations, or true but scientifically irrelevant local fluctuations. The smoothing operation removes precisely these high-frequency components, leaving the large-scale association structure that both normalizations agree upon. This convergence at consistent geometric scales indicates that the choice of weighting scheme becomes largely immaterial after appropriate smoothing. Both smoothed unit-weighted and smoothed derivative-weighted coefficients provide equally defensible measures of association structure. We adopt smoothed derivative-weighted coefficients for subsequent analyses, as derivative weighting naturally adapts to local manifold geometry, but we acknowledge this choice is pragmatic rather than definitive.

4.6 Matrix Extension for Multivariate Analysis

In practice, we rarely analyze a single predictor in isolation. Microbiome studies measure hundreds of bacterial taxa, genomic studies measure thousands of genes, and network data involve numerous node attributes. We require efficient computation of co-monotonicity between an outcome and multiple features, as well as among features themselves.

Let $y : V \rightarrow \mathbb{R}$ be an outcome function and $Z = [z_1, \dots, z_m] : V \rightarrow \mathbb{R}^m$ be a matrix of m feature functions. The co-monotonicity matrix between y and Z is the $n \times m$ matrix

$$\text{CM}(y, Z) = [\text{cm}(y, z_j; w)(v)]_{v \in V, j=1, \dots, m}, \quad (32)$$

where each column j contains the vertex-wise co-monotonicity coefficients between y and feature z_j . This matrix provides association profiles: row v shows how all features associate with the outcome in the neighborhood of vertex v , while column j shows the spatial pattern of association for feature z_j across all vertices.

Computing $\text{CM}(y, Z)$ naively by m independent calls to the pairwise co-monotonicity function would redundantly recompute edge differences $\Delta_e y$ for each feature. We optimize by precomputing these y -dependent quantities once, then reusing them across all features. The algorithm maintains edge weights w_e and differences $\Delta_e y$ in memory, iterates over features z_j , and for each feature computes $\Delta_e z_j$ and accumulates weighted products. This reduces

computational cost from $O(m \cdot |E|)$ operations with independent overhead to $O(|E| + m \cdot |E|)$ with shared preprocessing, yielding substantial savings when m is large.

For feature-feature associations, we compute the tensor

$$\text{CM}(Z, Z) = [\text{cm}(z_j, z_k; w)(v)]_{v \in V, j, k=1, \dots, m}, \quad (33)$$

which is an $n \times m \times m$ object containing co-monotonicity between all pairs of features at all vertices. The slice $\text{CM}(Z, Z)[v, :, :]$ is an $m \times m$ matrix showing how features co-vary in the neighborhood of vertex v . This captures local correlation structure in the feature space, revealing whether features cluster into modules that vary coherently or whether feature relationships differ across regions of the graph.

In applications, we augment $\text{CM}(y, Z)$ with selected columns from $\text{CM}(Z, Z)$ to form an extended association profile. For a vertex v , this profile includes both $\text{cm}(y, z_j)(v)$ for all features j and $\text{cm}(z_j, z_k)(v)$ for pairs (j, k) of interest. These profiles embed vertices into an association space where proximity reflects similarity in how outcome and features relate locally. Vertices with similar profiles form co-monotonicity cells, which we will explore in Section 5 as a basis for geometric multiple testing and biclustering.

4.7 Alternative Normalizations

The correlation-type co-monotonicity coefficient developed in Sections 4.2-4.4 employs Pearson-style normalization, dividing by the geometric mean of squared variations. This normalization provides stable estimates and interpretable coefficients bounded in $[-1, 1]$ for most applications. However, specific data characteristics or inferential goals may suggest alternative normalization schemes. We examine three such alternatives, providing concrete examples that illustrate when each approach succeeds or fails.

We begin by considering absolute value normalization, which divides the sum of weighted products by the sum of weighted absolute products. For edge weights w_e , this yields

$$\text{cm}_{\text{abs}}(y, z; w)(v) = \frac{\sum_{u \in N(v)} w_e \Delta_e y \cdot \Delta_e z}{\sum_{u \in N(v)} w_e |\Delta_e y \cdot \Delta_e z|}. \quad (34)$$

This normalization has intuitive interpretation: it measures the balance between concordant edges (positive products) and discordant edges (negative products), weighted by the magnitude of their products. When all edges show agreement, the numerator equals the denominator and $\text{cm}_{\text{abs}} = 1$. When disagreements exactly balance agreements in product-weighted terms, the coefficient vanishes.

The critical weakness of absolute value normalization emerges when one function varies sparsely. Consider a vertex v with 30 neighbors where the outcome y exhibits variation of magnitude 0.1 across all edges, while feature z shows meaningful variation (magnitude 0.1) on only one edge and remains essentially constant (changes < 0.01) on the remaining 29 edges. The single edge with signal contributes product ± 0.01 to the numerator. The 29 near-constant edges contribute products near zero. The denominator sums the absolute values of these products, yielding approximately $0.01 + 29 \times 0.001 = 0.039$. The resulting

coefficient is $\pm 0.01/0.039 \approx \pm 0.26$, suggesting moderate association despite signal appearing on only $1/30 \approx 3\%$ of edges. As the non-signal edges become exactly constant, the coefficient approaches ± 1 , indicating perfect association based on a single edge. This instability arises because the denominator can become arbitrarily small when one function is nearly constant, allowing sparse signal to dominate the measure.

Sign-based normalization addresses magnitude sensitivity by considering only directional information. We replace the weighted sums with counts of edges showing agreement versus disagreement:

$$\text{cm}_{\text{sign}}(y, z)(v) = \frac{\sum_{u \in N(v)} \text{sign}(\Delta_e y \cdot \Delta_e z)}{|N(v)|}, \quad (35)$$

where $\text{sign}(x) = 1$ if $x > 0$, $\text{sign}(x) = -1$ if $x < 0$, and $\text{sign}(0) = 0$. This coefficient measures the proportion of edges where functions agree in direction minus the proportion where they disagree, treating all edges equally regardless of change magnitude.

Sign-based normalization discards potentially valuable information about the strength of associations. Consider two scenarios at a vertex with 20 neighbors. In the first scenario, y and z both change by 0.5 units in the same direction on 11 edges and in opposite directions on 9 edges, yielding substantial co-variation with correlation 0.7. In the second scenario, y changes by 0.5 units on all edges while z shows tiny changes of 0.01 units in directions that happen to align with y on 11 edges and oppose y on 9 edges, exhibiting negligible true co-variation. The sign-based coefficient produces $(11 - 9)/20 = 0.1$ in both cases, treating large coordinated changes identically to small random fluctuations. The magnitude information that distinguishes biologically meaningful co-variation from numerical noise is completely lost. Moreover, sign-based coefficients remain vulnerable to the sparse signal problem: when z varies on only one edge, that single edge's sign determines the coefficient, yielding values of $\pm 1/|N(v)|$ that overstate association strength relative to the prevalence of signal.

These limitations of absolute value and sign-based normalizations arise from their treatment of edges with weak or absent signal. The absolute value denominator becomes small when products are small, amplifying sparse signals. The sign-based approach counts edges with arbitrarily weak variation equally with edges showing strong variation, obscuring signal strength. In practice, neither normalization provides reliable inference for heterogeneous data where features exhibit spatially varying signal intensity. We do not recommend their use in applications requiring robust, interpretable association measures.

For scenarios involving sparse or binary features where explicit signal filtering is scientifically justified, we introduce proportion-based co-monotonicity with thresholds. This measure explicitly filters edges by signal strength before aggregating directional agreements. Given threshold parameters $\tau_y, \tau_z > 0$, we assign each edge $e = [v, u]$ a directional agreement score:

$$s_e = \begin{cases} +1 & \text{if } |\Delta_e y| > \tau_y, |\Delta_e z| > \tau_z, \text{ and } \Delta_e y \cdot \Delta_e z > 0 \\ -1 & \text{if } |\Delta_e y| > \tau_y, |\Delta_e z| > \tau_z, \text{ and } \Delta_e y \cdot \Delta_e z < 0 \\ 0 & \text{otherwise.} \end{cases} \quad (36)$$

The proportion-based coefficient at vertex v is then

$$\text{cm}_{\text{prop}}(y, z; \tau_y, \tau_z)(v) = \frac{1}{|N(v)|} \sum_{e \in N(v)} s_e, \quad (37)$$

where the sum is over all edges incident to v , and $|N(v)|$ denotes the total number of neighbors. Edges where either function shows insufficient variation (below threshold) contribute zero rather than being excluded from the denominator.

The key distinction from previous measures lies in how sparse signal is handled. Return to the vertex with 30 neighbors where y varies on all edges but z shows meaningful signal on only one edge. Setting thresholds $\tau_y = \tau_z = 0.05$ appropriate for the variation scales, the proportion-based measure yields $\text{cm}_{\text{prop}}(y, z)(v) = \pm 1/30 \approx \pm 0.033$. This value correctly indicates that association is supported by sparse evidence: only 3% of the neighborhood exhibits coordinated variation. As more edges develop signal, the coefficient magnitude increases proportionally, reaching ± 1 only when directional concordance appears across the entire neighborhood. The fixed denominator prevents sparse signals from producing misleadingly large coefficients while maintaining interpretability as the proportion of edges showing directional agreement.

Threshold selection depends on data characteristics and inferential goals. For the response function y , thresholds can be set relative to overall variation: $\tau_y = c \cdot \text{sd}(y)$ for small c (typically 0.05 to 0.10) filters changes smaller than 5 – 10% of a standard deviation, removing numerical noise while preserving meaningful signal. For feature z representing quantities like phylotype abundances that vary heterogeneously across features, adaptive per-feature thresholds based on quantiles of edge differences prove effective. Setting $\tau_{z_j} = Q_{0.25}(\{|\Delta_e z_j| : e \in E\})$ as the first quartile of absolute edge differences for feature z_j filters the bottom 25% of changes as noise while preserving variation in the upper three quartiles. This adaptive approach handles features with different baseline variability without requiring manual tuning. When thresholds are set to zero ($\tau_y = \tau_z = 0$), the proportion-based measure reduces to the sign-based coefficient, recovering pure directional counting without magnitude filtering.

The proportion-based measure is particularly appropriate for binary or sparse features where the presence or absence of variation carries biological meaning. In microbiome studies, phylotypes may be absent from most samples but abundant where present, exhibiting extreme sparsity. The proportion-based coefficient with appropriate thresholds identifies regions where a phylotype’s presence correlates with outcome changes while appropriately penalizing associations supported by few samples. For continuous features exhibiting widespread variation, the correlation-type measure from Section 4.2 generally provides more sensitive detection of graded co-variation by weighting edges according to the magnitude of coordinated changes.

We summarize the comparison between normalization schemes. The correlation-type measure cm_{cor} employs geometric mean normalization that provides stable coefficients across diverse signal patterns, interprets naturally as correlation between discrete derivatives, and weights edges by the magnitude of coordinated variation. It is recommended for general use with continuous features exhibiting heterogeneous but widespread variation. The proportion-based measure cm_{prop} with thresholds explicitly filters weak signals, interprets

as the proportion of neighborhood edges showing directional agreement, and naturally handles sparse or binary features where signal prevalence matters. It is recommended when explicit signal filtering is scientifically justified or when features exhibit extreme sparsity. The absolute value normalization cm_{abs} becomes unstable with sparse signals and is not recommended for practical use. The sign-based normalization cm_{sign} discards magnitude information that typically proves essential for distinguishing meaningful associations from noise and is not recommended for practical use. In applications where the choice is unclear, we suggest computing both cm_{cor} and cm_{prop} with conservative thresholds, examining their agreement to assess whether magnitude weighting versus prevalence counting yields substantively different conclusions.

5. Statistical Inference for Co-Monotonicity

Having developed co-monotonicity coefficients as geometric measures of directional association, we confront the fundamental inferential question: how should we distinguish genuine associations from artifacts of sampling variability? The vertex-wise nature of co-monotonicity coefficients presents both opportunity and challenge. We obtain spatially resolved information revealing where associations are strongest, but this spatial resolution demands vertex-level inference procedures that respect the graph structure while accounting for multiple comparisons. The standard hypothesis testing framework, with its focus on p -values and frequentist error rates, sits uncomfortably with the Bayesian spectral filtering that produces smoothed function estimates. We require inference procedures that propagate uncertainty from the estimation stage through to association quantification, providing probabilistic statements about effect sizes rather than merely rejecting null hypotheses.

5.1 The Multiple Testing Challenge

Consider the typical scenario in microbiome-outcome association studies. We have n samples (vertices in the graph G), an outcome $y : V \rightarrow \mathbb{R}$, and m bacterial taxa (features) $Z = [z_1, \dots, z_m] : V \rightarrow \mathbb{R}^m$. After smoothing to obtain \hat{y} and \hat{Z} through spectral filtering, we compute the co-monotonicity matrix $\text{CM}(\hat{y}, \hat{Z}) \in \mathbb{R}^{n \times m}$ with $n \times m$ coefficients. A naive testing procedure would assess each coefficient independently: for each vertex-feature pair (v, j) , test whether $\text{cm}(\hat{y}, z_j)(v)$ differs significantly from zero. This generates nm hypothesis tests, and with typical values $n = 200$ samples and $m = 100$ features, we face 20,000 simultaneous tests.

The multiple testing burden is severe. Even with independent tests, controlling the family-wise error rate at level $\alpha = 0.05$ through Bonferroni correction requires declaring significance only when $p < 0.05/20000 = 2.5 \times 10^{-6}$, a threshold so stringent that only the most extreme associations would be detected. False discovery rate control offers less conservative correction but still penalizes for the sheer number of tests. Moreover, the independence assumption underlying standard FDR procedures fails dramatically in our setting: co-monotonicity coefficients at adjacent vertices are inherently correlated because they aggregate over overlapping neighborhoods. The graph structure induces spatial dependence that standard multiple testing corrections ignore.

Beyond the computational burden of multiple testing, there is a conceptual issue. The classical hypothesis testing framework asks whether we can reject the null hypothesis of no association, yielding binary decisions (reject or fail to reject) with probabilistic error control. Yet in exploratory high-dimensional data analysis, we rarely seek such binary classifications. We wish to identify regions where associations are strongest, quantify the magnitude of these associations with uncertainty bounds, and compare the strength of different feature-outcome relationships. The hypothesis testing paradigm, with its focus on p -values that measure tail probabilities under null distributions, provides limited information for these goals. We require inference methods that directly address probabilistic questions about effect sizes: what is $P(|\text{cm}(\hat{y}, z_j)(v)| > \delta \mid \text{data})$ for scientifically meaningful thresholds δ , rather than merely $P(\text{data} \mid \text{cm} = 0)$?

5.2 Vertex-Wise Permutation Testing

We begin with the classical nonparametric approach to association testing. Permutation tests provide exact finite-sample inference without distributional assumptions, making them particularly appealing for complex data structures. The key insight is that under the null hypothesis of no association between feature z and outcome y , permuting the feature values across vertices should preserve all aspects of the data generation process except the association of interest.

At each vertex v , we test the null hypothesis $H_0^v : \text{cm}(y, z)(v) = 0$, which corresponds to asserting that y and z have no directional relationship in the neighborhood of v . We compute the observed coefficient $c_{\text{obs}}(v) = \text{cm}(\hat{y}, \hat{z})(v)$ using the smoothed estimates. To generate the null distribution, we permute the feature values: let π be a random permutation of $\{1, \dots, n\}$, and define the permuted feature $z^\pi(v_i) = z(v_{\pi(i)})$ for $i = 1, \dots, n$. This permutation breaks any association between z and y while preserving the marginal distribution of z and the graph structure G .

For each permutation π_b with $b = 1, \dots, B$, we smooth the permuted feature to obtain $\hat{z}^{(\pi_b)}$ and compute $c_b(v) = \text{cm}(\hat{y}, \hat{z}^{(\pi_b)})(v)$. The collection $\{c_1(v), \dots, c_B(v)\}$ forms an empirical null distribution for the co-monotonicity coefficient at vertex v under the hypothesis of no association. We compute the two-sided p -value as

$$p(v) = \frac{1 + \#\{b : |c_b(v)| \geq |c_{\text{obs}}(v)|\}}{B + 1}, \quad (38)$$

where the numerator counts permutations yielding coefficients at least as extreme as the observed value, and the denominator includes the observed data itself as one possible permutation.

This vertex-wise permutation procedure respects the graph structure: the permuted features are smoothed using the same spectral filtering as the original data, ensuring that the null distribution reflects the spatial autocorrelation induced by the Laplacian. However, the procedure treats the smoothed outcome \hat{y} as fixed, ignoring the uncertainty in its estimation. When y itself is estimated through spectral filtering of noisy observations, this omission can lead to underestimation of uncertainty and inflated false positive rates.

For multiple testing correction across the n vertices, we employ the Benjamini-Hochberg procedure to control the false discovery rate. Order the p -values as $p_{(1)} \leq p_{(2)} \leq \dots \leq p_{(n)}$, and let k^* be the largest k such that $p_{(k)} \leq (k/n)\alpha$ for target FDR level α . We declare vertices v with $p(v) \leq p_{(k^*)}$ as significant. This procedure controls the expected proportion of false discoveries among the rejected hypotheses, providing a less conservative alternative to family-wise error rate control.

The spatial structure of significant vertices provides additional information. Rather than treating each vertex independently, we identify connected components in the subgraph induced by significant vertices. Isolated significant vertices likely represent false positives that happened to achieve small p -values by chance, while spatially coherent clusters of significant vertices suggest genuine regional associations. We can impose a minimum cluster size threshold, declaring only those significant vertices belonging to clusters of at least k_{\min} vertices as discoveries. This spatial thresholding provides robustness against false positives arising from the multiple testing burden.

5.3 Bayesian Inference via Posterior Sampling

The permutation testing framework, despite its nonparametric appeal, inherits the limitations of the classical hypothesis testing paradigm. We now develop an alternative Bayesian approach that addresses these limitations by treating uncertainty in the smoothed estimates as the primary source of inferential variability.

The spectral filtering procedure that produces smoothed estimates \hat{y} and \hat{Z} from observed data y and Z admits natural Bayesian interpretation. Recall that the filtered estimate takes the form $\hat{y} = VF_\eta(\Lambda)V^T y$, where V contains eigenvectors of the normalized Laplacian, Λ is the diagonal matrix of eigenvalues, and F_η is a spectral filter (such as the heat kernel $F_\eta(\lambda) = \exp(-\eta\lambda)$ or Tikhonov filter $F_\eta(\lambda) = 1/(1 + \eta\lambda)$). This operation corresponds to the posterior mean under a Gaussian prior on spectral coefficients with precision proportional to eigenvalues.

We elaborate this Bayesian perspective through a generative model for the observed data. Suppose the true outcome function $f : V \rightarrow \mathbb{R}$ has spectral representation $f = V\alpha$ for coefficients $\alpha \in \mathbb{R}^m$, where m is the number of eigenvectors retained. The smoothness prior on spectral coefficients is

$$p(\alpha \mid \eta) \propto \exp\left(-\frac{\eta}{2} \sum_{j=1}^m \lambda_j \alpha_j^2\right), \quad (39)$$

which penalizes high-frequency modes (large λ_j) more severely. Given noisy observations $y_v = f(v) + \epsilon_v$ with $\epsilon_v \sim N(0, \sigma^2)$, the posterior distribution over spectral coefficients is Gaussian:

$$\alpha \mid y, \eta \sim N\left((I + \eta\Lambda)^{-1}V^T y, \sigma^2(I + \eta\Lambda)^{-1}\right). \quad (40)$$

The filtered estimate $\hat{y} = VF_\eta(\Lambda)V^T y$ computes the posterior mean when $F_\eta(\lambda) = 1/(1 + \eta\lambda)$. For other filter types, the filtered estimate approximates the posterior mode or mean

under related priors. This connection suggests a natural approach to uncertainty quantification: sample from the posterior distribution over spectral coefficients, transform to vertex space, and propagate this uncertainty through the co-monotonicity computation.

However, directly sampling from the spectral coefficient posterior requires estimating the residual variance σ^2 and assumes Gaussian noise, which may not hold for discrete or bounded outcomes. We employ an alternative resampling strategy that induces posterior-like variability without requiring parametric assumptions. The key idea is to perturb the vertex masses in the Riemannian structure through Dirichlet resampling, generating multiple weighted Laplacians that yield different smoothed estimates.

Definition 1 (Dirichlet Resampling for Posterior Uncertainty). Let M_0 be the vertex mass matrix with diagonal entries $M_0[v, v] = \rho_0(v)$. Denote $w = (\rho_0(1)/n, \dots, \rho_0(n)/n)$ as the normalized vertex weights summing to unity. For concentration parameter $\alpha > 0$, we sample

$$w^* \sim \text{Dirichlet}(\alpha w_1, \dots, \alpha w_n), \quad (41)$$

where larger α concentrates the resampled weights near the original weights w , and smaller α allows greater variability. We construct a perturbed mass matrix M_0^* with diagonal entries $M_0^*[v, v] = n w_v^*$, build the corresponding weighted Laplacian L^* , and compute filtered estimates $\hat{y}^* = V^* F_\eta(\Lambda^*) (V^*)^T y$ and $\hat{z}_j^* = V^* F_\eta(\Lambda^*) (V^*)^T z_j$, where V^* and Λ^* come from the eigendecomposition of L^* .

This Dirichlet resampling procedure induces variability in the smoothed estimates through perturbation of the geometric structure itself. Vertices with large mass $\rho_0(v)$ tend to receive large perturbed mass $M_0^*[v, v]$, but stochastic variation allows for reordering of vertex importance across samples. The resulting ensemble $\{(\hat{y}^{(b)}, \hat{z}^{(b)})\}_{b=1}^B$ for B independent Dirichlet samples approximates a posterior distribution over smoothed functions.

For each posterior sample b , we compute co-monotonicity coefficients $c^{(b)}(v) = \text{cm}(\hat{y}^{(b)}, \hat{z}_j^{(b)})(v)$ at each vertex v and for each feature j . The empirical distribution of $\{c^{(1)}(v), \dots, c^{(B)}(v)\}$ represents the posterior distribution of the co-monotonicity coefficient at vertex v . We construct credible intervals by computing empirical quantiles: the $(1 - \alpha) \times 100\%$ credible interval for $\text{cm}(\hat{y}, z_j)(v)$ is

$$\text{CI}_{1-\alpha}(v) = [q_{\alpha/2}(\{c^{(b)}(v)\}), q_{1-\alpha/2}(\{c^{(b)}(v)\})], \quad (42)$$

where q_p denotes the p -quantile of the empirical distribution.

These Bayesian credible intervals admit direct probability interpretation: given the observed data and the smoothness prior implicit in spectral filtering, there is $(1 - \alpha) \times 100\%$ posterior probability that the true co-monotonicity lies within the interval. This contrasts with frequentist confidence intervals, which make statements about long-run coverage under repeated sampling. For a vertex v where the credible interval excludes zero (say, $\text{CI}_{0.95}(v) = [0.42, 0.71]$), we conclude with high posterior probability that a genuine directional association exists in the neighborhood of v , and the interval quantifies the magnitude of this association.

5.4 Posterior Probabilities for Effect Size Thresholds

Beyond credible intervals, the Bayesian framework enables computation of posterior probabilities for scientifically meaningful thresholds. Rather than testing whether $\text{cm}(\hat{y}, z)(v) = 0$, we ask whether the co-monotonicity exceeds a threshold $\delta > 0$ representing meaningful association strength. For example, in microbiome studies, we might consider $|\text{cm}| > 0.3$ as indicating moderate directional concordance, and $|\text{cm}| > 0.6$ as strong concordance.

The posterior probability that the co-monotonicity at vertex v exceeds threshold δ is estimated from the empirical distribution of posterior samples:

$$P(|\text{cm}(\hat{y}, z)(v)| > \delta \mid \text{data}) \approx \frac{1}{B} \#\{b : |c^{(b)}(v)| > \delta\}. \quad (43)$$

This probability directly quantifies our belief that the association is meaningful, given the data and prior assumptions. A vertex with $P(|\text{cm}| > 0.3 \mid \text{data}) = 0.95$ has high posterior support for at least moderate association, while $P(|\text{cm}| > 0.6 \mid \text{data}) = 0.45$ indicates uncertain evidence for strong association.

This formulation avoids the binary decision problem inherent in hypothesis testing. We need not declare associations as significant or non-significant based on arbitrary α levels; instead, we report posterior probabilities and credible intervals, allowing domain experts to interpret the strength of evidence in context. Moreover, the Bayesian framework naturally handles multiple comparisons without explicit correction procedures. The posterior distribution already accounts for all sources of uncertainty, including estimation variability and the fact that we are simultaneously assessing many vertex-feature pairs. There is no multiplicity penalty in the Bayesian paradigm because we report probabilistic statements about effect sizes rather than making decisions about null hypotheses.

5.5 Comparison of Inference Approaches

The permutation testing and Bayesian posterior sampling approaches address the inferential challenge from fundamentally different perspectives. We summarize their complementary strengths and limitations.

Permutation testing provides distribution-free inference with exact finite-sample control of type I error rates. Under the null hypothesis of no association, the permutation distribution correctly represents the sampling variability of the test statistic, regardless of the underlying data distribution. This makes permutation tests particularly robust in settings where parametric assumptions are dubious. The vertex-wise procedure respects the graph structure by applying the same spectral filtering to permuted features as to the original data. For confirmatory hypothesis testing where strict control of false positive rates is paramount, permutation tests offer theoretical guarantees that Bayesian methods cannot match.

However, permutation testing treats the smoothed outcome \hat{y} as fixed, ignoring uncertainty in its estimation. When y itself arises from noisy observations and requires smoothing, this omission understates the true uncertainty. The resulting p -values may be anticonservative (too small), inflating false positive rates beyond the nominal level. Moreover, permutation

testing yields p -values rather than effect size estimates, requiring separate procedures for quantifying association strength with confidence intervals. The multiple testing correction necessary for controlling FDR or FWER across vertices introduces additional complexity and reduces power, particularly when spatial dependence invalidates independence assumptions underlying standard corrections.

Bayesian posterior sampling addresses these limitations by treating estimation uncertainty as the primary source of inferential variability. The Dirichlet resampling procedure perturbs the geometric structure itself, inducing correlated variability across all smoothed functions. This naturally propagates uncertainty from the estimation stage to the association quantification stage, providing credible intervals that reflect both sampling variability and smoothing uncertainty. The resulting inference is more conservative (wider intervals) but also more honest about what the data truly support. The Bayesian framework yields direct probabilistic statements about effect sizes, such as $P(|cm| > 0.3 \mid \text{data})$, which answer the scientific questions investigators actually care about.

The disadvantage of Bayesian inference is the need to specify the resampling mechanism (the concentration parameter α in Dirichlet sampling) and the interpretation depends on accepting the implicit prior structure. While the Bayesian credible intervals have asymptotically correct frequentist coverage under regularity conditions (the intervals do contain the true parameter with the stated frequency in repeated sampling), this property requires assumptions about the smoothing operator and the data-generating process. For small samples or when these assumptions fail, Bayesian intervals may not achieve nominal coverage.

We recommend a pragmatic approach that leverages both methods. For exploratory analysis and effect size estimation, employ Bayesian posterior sampling to obtain credible intervals and posterior probabilities. The resulting summaries provide rich information about association patterns, enabling investigators to identify regions of strong association, quantify uncertainty, and compare effects across features. For confirmatory testing where false positive control is critical, supplement the Bayesian analysis with permutation tests, applying FDR correction and spatial thresholding to protect against spurious discoveries. The convergence of evidence from both frameworks strengthens confidence in reported associations.

5.6 Handling Spatial Dependence

Both inference approaches must confront the spatial dependence inherent in co-monotonicity coefficients on graphs. Adjacent vertices typically have similar coefficient values because their neighborhoods overlap, creating positive correlation that standard multiple testing procedures ignore. This spatial autocorrelation inflates the effective number of independent tests, making nominal FDR control procedures liberal (actual FDR exceeds target level).

For permutation testing, we can adapt spatial FDR methods developed for neuroimaging and spatial statistics. One approach treats the significant vertices as a spatial point process and controls the false discovery rate accounting for spatial clustering. We compute the expected number of false positive clusters under the null distribution by examining the

spatial distribution of significant vertices in permuted data, then calibrate the rejection threshold to achieve the desired spatial FDR. Alternatively, we can employ random field theory, modeling the co-monotonicity surface as a Gaussian random field and deriving familywise error rates for the maximum statistic over connected regions. These methods require assumptions about the spatial correlation structure but provide more powerful inference than Bonferroni correction when correctly specified.

For Bayesian inference, spatial dependence manifests in the posterior distribution of co-monotonicity vectors across vertices. We can examine the posterior covariance between coefficients at different vertices, identifying regions where association patterns are consistently similar across posterior samples. High posterior correlation between nearby vertices supports the interpretation that they belong to a coherent association region rather than representing independent local effects. This spatial coherence can inform downstream analyses such as biclustering, where we seek to partition vertices into regions based on their association profiles.

A pragmatic approach to spatial dependence is cluster-based inference: rather than testing individual vertices, we test connected components of vertices with large coefficients. The null hypothesis becomes "no cluster of associated vertices exists" rather than "no individual vertex is associated." We compute a cluster-level test statistic (such as the sum of co-monotonicity coefficients within the cluster) and generate its null distribution through permutation. This reduces the multiple testing burden from n vertex-level tests to k cluster-level tests where $k \ll n$, and the spatial thresholding inherent in cluster definition provides robustness against isolated false positives.

5.7 Return to the Motivating Challenge

We return to the multiple testing scenario described in the opening: $n = 200$ samples, $m = 100$ features, yielding 20,000 vertex-feature pairs to assess. Under the permutation testing framework with Benjamini-Hochberg FDR control at level $\alpha = 0.05$, we might identify 500 significant pairs, corresponding to roughly 2.5% of the total. These discoveries typically cluster spatially, with certain vertices showing strong association with multiple features and certain features showing strong association across multiple vertices. The spatial thresholding ensures that we report coherent regions rather than scattered individual vertices.

Under the Bayesian framework, we report the full posterior distribution of co-monotonicity coefficients, providing credible intervals for all 20,000 pairs. For a scientist examining feature j , we can visualize the posterior mean $\text{cm}(\hat{y}, z_j)(v)$ across vertices v , shading regions where the 95% credible interval excludes zero. The width of intervals reveals uncertainty: narrow intervals in densely sampled regions with consistent associations, wide intervals in sparse or heterogeneous regions. Rather than a binary classification of significant versus non-significant, we obtain a graduated assessment of association strength and certainty across the entire sample space.

The two approaches yield complementary information. Permutation testing with FDR control provides a specific set of discoveries with guaranteed error rate properties, suitable for reporting in publications and for guiding follow-up experiments where false positive

costs are high. Bayesian credible intervals provide nuanced effect size estimates with uncertainty quantification, enabling investigators to prioritize regions for mechanistic investigation based on both the strength of association and the confidence in that strength. Together, these tools enable rigorous yet flexible inference that respects the geometric structure of the data while controlling error rates and propagating uncertainty.

6. Geometric Multiple Testing via Co-Monotonicity Cells

The vertex-wise inference procedures developed in the previous section enable assessment of individual vertex-feature associations, but they address only part of the inferential challenge. When examining co-monotonicity heatmaps from real applications, a striking pattern emerges: coefficients organize into coherent blocks where groups of vertices exhibit similar association patterns with groups of features. This block structure suggests that regional associations operate not through individual vertex-feature pairs but through collective relationships between sample regions and feature modules. We require a framework that discovers this geometric structure directly, partitioning both the sample space and feature space simultaneously to identify co-monotonicity cells where multivariate associations are coherent.

6.1 The Context-Dependent Association Problem

Consider a microbiome study investigating associations between bacterial taxa and spontaneous preterm birth outcomes. We compute the co-monotonicity matrix $CM(\hat{y}, \hat{Z}) \in \mathbb{R}^{n \times m}$ where rows correspond to samples (vertices in the graph G constructed from high-dimensional feature profiles) and columns correspond to bacterial phylotypes. Figure 3 displays such a matrix from a study of vaginal microbiome composition in pregnant women, with hierarchical clustering applied to both rows and columns to reveal structure.

The heatmap reveals a block pattern that standard vertex-wise testing cannot capture. One block of samples (upper portion) exhibits strong positive co-monotonicity (red) between outcome and certain phylotypes, indicating these bacteria increase when preterm birth risk increases. A different block of samples (middle portion) shows weak or negative association (blue/yellow) between outcome and the same phylotypes. A third block shows intermediate patterns. Similarly, phylotypes organize into modules: certain taxa co-vary strongly with the outcome across specific sample regions but not others, while different taxa exhibit complementary patterns.

This structure poses fundamental challenges for conventional inference approaches. Testing each phylotype separately across all samples conflates the regional signals, potentially concluding that a phylotype shows no global association when in fact it exhibits strong positive association in one region and strong negative association in another. The signals cancel in global analysis, yielding small test statistics and large p -values despite genuine context-dependent effects. Stratifying by known covariates (such as community state type

in microbiome studies) helps but requires investigators to specify strata a priori, and may miss finer-scale heterogeneity within nominal strata.

Moreover, examining individual phlotypes ignores valuable information about their collective behavior. If ten phlotypes all show moderate positive co-monotonicity ($\text{cm}(\hat{y}, z_i)(v) \approx 0.5$) in the same sample region, the coherence across multiple features provides stronger evidence for genuine association than any single phlotype achieves alone. The features form a functional module that operates together, and inference should leverage this coordinated behavior. Traditional multiple testing corrections treat each feature independently, applying penalties that ignore the reduced effective number of independent tests when features cluster into modules.

We seek a framework that addresses both challenges simultaneously: discovering regions where associations differ while identifying feature modules that exhibit coordinated relationships with outcomes within those regions. This leads naturally to biclustering, which partitions rows (samples) and columns (features) simultaneously to maximize within-block homogeneity and between-block heterogeneity.

6.2 Co-Monotonicity Embeddings into Association Space

The co-monotonicity matrix $\text{CM}(\hat{y}, \hat{Z})$ provides association information for each vertex-feature pair, but to discover regional structure, we require a representation that captures the complete association profile at each vertex. We construct embeddings that transform vertices into points in an association space where geometric proximity reflects similarity in how features relate to outcomes.

The simplest embedding uses outcome-feature associations directly. For each vertex v , we form the association profile vector

$$\text{cm}(\hat{y}, \hat{Z})(v) = [\text{cm}(\hat{y}, z_1)(v), \dots, \text{cm}(\hat{y}, z_m)(v)]^T \in \mathbb{R}^m, \quad (44)$$

which concatenates the co-monotonicity coefficients between outcome and all features at vertex v . This m -dimensional vector summarizes how the outcome associates with each feature in the neighborhood of v . Vertices with similar profiles have similar association patterns, while vertices with dissimilar profiles exhibit different feature-outcome relationships.

This outcome-centric embedding captures one aspect of association structure, but it omits information about how features relate to each other. Two vertices might have similar outcome-feature profiles (similar co-monotonicity with \hat{y} for each feature) yet exhibit different inter-feature correlation patterns. In one region, features z_i and z_j might co-vary positively (both increase together), while in another region they vary independently or negatively. These inter-feature relationships reveal mechanistic structure: positively co-monotonic feature pairs may participate in the same biological pathway or competitive network, and regional differences in inter-feature associations indicate distinct underlying processes.

We therefore construct an augmented embedding that incorporates inter-feature associations. For each vertex v , compute the pairwise co-monotonicity $\text{cm}(z_i, z_j)(v)$ for all feature

pairs $i < j$, yielding $\binom{m}{2} = m(m-1)/2$ coefficients. Concatenate these with the outcome-feature associations to form the augmented profile

$$\widetilde{\text{cm}}(\hat{y}, \hat{Z})(v) = \begin{bmatrix} \text{cm}(\hat{y}, z_1)(v) \\ \vdots \\ \text{cm}(\hat{y}, z_m)(v) \\ \text{cm}(z_1, z_2)(v) \\ \vdots \\ \text{cm}(z_{m-1}, z_m)(v) \end{bmatrix} \in \mathbb{R}^{m+m(m-1)/2}. \quad (45)$$

This augmented representation has dimension $m + \binom{m}{2} = m(m+1)/2$, which grows quadratically in the number of features. For $m = 100$ features, the augmented embedding has dimension 5,050. While high-dimensional, this representation preserves complete pairwise association structure, enabling discovery of regions where both outcome associations and feature co-variation patterns differ.

The augmented embedding offers several advantages over the outcome-only version. It captures mechanistic information: vertices clustered together in the augmented space share not only similar outcome associations but also similar inter-feature dependencies, suggesting common underlying processes. It enables multi-modal integration: when analyzing multiple feature sets (genomic, proteomic, metabolomic), we can augment the embedding with cross-modal associations, identifying regions where different data types exhibit coordinated relationships. It provides robustness: even when outcome-feature associations are weak, strong inter-feature structure can drive clustering, revealing latent organization that outcome-only embeddings would miss.

6.3 Graph Construction in Association Space

Given the co-monotonicity embedding $\widetilde{\text{cm}}(\hat{y}, \hat{Z}) : V \rightarrow \mathbb{R}^d$ where $d = m(m+1)/2$, we construct a new graph $G_k(\text{cm})$ in the association space. For each vertex $v \in V$, we identify its k nearest neighbors in \mathbb{R}^d using Euclidean distance on the embedded coordinates. This yields a graph where edge $[u, v] \in E(G_k(\text{cm}))$ indicates that vertices u and v have similar association profiles, with proximity measured directly in terms of co-monotonicity coefficients rather than in the original high-dimensional feature space.

The choice of k controls the granularity of the induced structure. Small k produces a sparse graph capturing only the most similar association profiles, potentially fragmenting the vertex set into many disconnected components. Large k creates a dense graph where even moderately dissimilar profiles connect, potentially obscuring meaningful distinctions between regions. We employ the same principles developed for the original data graph construction: select k to ensure connectivity while maintaining local geometric fidelity, typically using k proportional to $\log n$ for n vertices.

The graph $G_k(\text{cm})$ provides a geometric representation of association structure. Communities in this graph (densely connected subgraphs with sparse connections between communities) correspond to co-monotonicity cells: regions where vertices exhibit similar association patterns. Unlike the original data graph G , which captures proximity in feature space

(microbiome composition, gene expression, etc.), the association graph $G_k(\text{cm})$ captures proximity in association space. Two samples far apart in microbiome composition might be close in association space if bacteria relate to outcomes similarly in both samples, revealing that similar mechanisms operate despite different baseline compositions.

6.4 Community Detection and Biclustering

We apply community detection algorithms to $G_k(\text{cm})$ to partition vertices into regions. The Louvain method provides an efficient modularity-based approach that scales to large graphs and naturally handles hierarchical structure through multi-resolution optimization. Given the graph $G_k(\text{cm})$ with edge weights derived from association profile similarities, the Louvain algorithm iteratively groups vertices to maximize the modularity function

$$Q = \frac{1}{2|E|} \sum_{[u,v] \in E} \left(A_{uv} - \frac{k_u k_v}{2|E|} \right) \delta(c_u, c_v), \quad (46)$$

where A_{uv} is the adjacency matrix, k_u is the degree of vertex u , c_u is the community assignment of u , and δ is the Kronecker delta. This optimization balances within-community edge density against the expected density under a null model, identifying communities more densely connected internally than would occur by chance.

The resulting partition $\{R_1, \dots, R_K\}$ divides vertices into K regions where association profiles are similar within regions and dissimilar between regions. The number of regions K emerges from the optimization rather than being specified a priori, and the hierarchical nature of Louvain clustering enables exploration of structure at multiple scales by varying the resolution parameter.

To identify feature modules, we transpose the analysis. Compute the similarity between feature columns in $\text{CM}(\hat{y}, \hat{Z})$: features z_i and z_j are similar if their co-monotonicity profiles across vertices $\text{cm}(\hat{y}, z_i)$ and $\text{cm}(\hat{y}, z_j)$ are correlated. This yields a feature similarity matrix that we cluster using hierarchical agglomerative clustering or network community detection. The resulting modules $\{S_1, \dots, S_M\}$ group features that exhibit similar spatial patterns of association with the outcome.

The combination of vertex regions and feature modules defines a bicluster structure $\{(R_j, S_k)\}_{j=1, \dots, K; k=1, \dots, M}$ partitioning the co-monotonicity matrix into $K \times M$ blocks. Each block (R_j, S_k) represents a co-monotonicity cell where vertices in region R_j exhibit coherent associations with features in module S_k . This structure reveals the regional organization of multivariate associations, showing which feature combinations drive outcomes in which sample contexts.

6.5 Bayesian Uncertainty Quantification for Biclusters

The biclustering procedure applied to a single estimate $\text{CM}(\hat{y}, \hat{Z})$ yields a point estimate of the partition structure, but this estimate is uncertain. Different choices of smoothing parameter, different posterior samples from the Bayesian inference framework, or different noise realizations would produce different clusterings. We require uncertainty quantification

for the discovered structure itself, characterizing our confidence in the identified regions and modules.

The posterior sampling framework developed in Section 5 provides a natural approach. For each Dirichlet-resampled weight vector $w^{(b)}$ with $b = 1, \dots, B$, we obtain smoothed estimates $\hat{y}^{(b)}$ and $\hat{Z}^{(b)}$, compute the corresponding co-monotonicity matrix $\text{CM}^{(b)}(\hat{y}, \hat{Z})$, and apply the biclustering procedure to obtain partition $\mathcal{P}^{(b)} = \{R_1^{(b)}, \dots, R_{K_b}^{(b)}\}$ of vertices and $\mathcal{S}^{(b)} = \{S_1^{(b)}, \dots, S_{M_b}^{(b)}\}$ of features. The ensemble $\{\mathcal{P}^{(1)}, \dots, \mathcal{P}^{(B)}\}$ represents the posterior distribution over vertex partition structures, and similarly for feature modules.

To summarize this distribution, we compute co-clustering probabilities. For each pair of vertices (u, v) , the posterior probability that they belong to the same region is

$$\pi_v(u, v) = P(u \text{ and } v \text{ in same region} \mid \text{data}) \approx \frac{1}{B} \sum_{b=1}^B \mathbb{I}\{u, v \in R_j^{(b)} \text{ for some } j\}, \quad (47)$$

where $\mathbb{I}\{\cdot\}$ is the indicator function. This probability quantifies our confidence that vertices u and v truly belong together based on their association profiles, accounting for all sources of uncertainty. High co-clustering probability ($\pi_v(u, v) > 0.95$) indicates strong evidence for grouping, while low probability ($\pi_v(u, v) < 0.20$) suggests the vertices belong to different regions.

Similarly, for each pair of features (z_i, z_j) , we compute

$$\pi_f(z_i, z_j) = P(z_i \text{ and } z_j \text{ in same module} \mid \text{data}) \approx \frac{1}{B} \sum_{b=1}^B \mathbb{I}\{z_i, z_j \in S_k^{(b)} \text{ for some } k\}. \quad (48)$$

These co-clustering probabilities enable construction of credible regions and modules. A credible region R at level $1 - \alpha$ satisfies $\pi_v(u, v) \geq 1 - \alpha$ for all pairs $u, v \in R$, meaning we have at least $(1 - \alpha) \times 100\%$ posterior probability that every pair in the region genuinely belongs together. Maximal credible regions (those not properly contained in any larger credible region) provide conservative summaries of the partition structure, reporting only clusters with high posterior support.

We can also examine the posterior distribution over the number of regions and modules. Let $K^{(b)}$ denote the number of regions in posterior sample b . The empirical distribution of $\{K^{(1)}, \dots, K^{(B)}\}$ quantifies uncertainty about the appropriate granularity of the partition. If this distribution concentrates sharply around a single value (say, $K = 5$ with probability 0.90), we have strong evidence for that many regions. If the distribution is diffuse (ranging from $K = 3$ to $K = 10$ with no dominant mode), the data do not provide clear guidance about the resolution, and we should report results at multiple scales.

6.6 Statistical Inference within Co-Monotonicity Cells

Having identified regions $\{R_1, \dots, R_K\}$ and modules $\{S_1, \dots, S_M\}$, we perform statistical inference on the region-module pairs (R_j, S_k) to assess the strength and uncertainty of associations within each cell. The fundamental question is whether features in module S_k

exhibit coherent association with the outcome among vertices in region R_j , and if so, how strong is this association.

We define the region-module coherence as the average absolute co-monotonicity within the cell:

$$\tau(R_j, S_k) = \frac{1}{|R_j| \cdot |S_k|} \sum_{v \in R_j} \sum_{i \in S_k} |\text{cm}(\hat{y}, z_i)(v)|. \quad (49)$$

This quantity measures the typical magnitude of association between outcome and features in the module, averaged over vertices in the region. Large $\tau(R_j, S_k)$ indicates strong coherent association, while small $\tau(R_j, S_k)$ suggests weak or inconsistent associations.

For each posterior sample b , we compute $\tau^{(b)}(R_j, S_k)$ using the posterior estimates $\hat{y}^{(b)}$ and $\hat{Z}^{(b)}$. The empirical distribution of $\{\tau^{(1)}(R_j, S_k), \dots, \tau^{(B)}(R_j, S_k)\}$ represents the posterior distribution of coherence for this cell. We construct a credible interval $[\tau_{\text{low}}, \tau_{\text{high}}]$ from the empirical quantiles and compute the posterior probability of meaningful coherence:

$$P(\tau(R_j, S_k) > \delta \mid \text{data}) \approx \frac{1}{B} \sum_{b=1}^B \mathbb{I}\{\tau^{(b)}(R_j, S_k) > \delta\}, \quad (50)$$

for a scientifically meaningful threshold δ (for example, $\delta = 0.5$ indicating moderate association on average).

This cell-level inference enjoys several advantages over vertex-wise or feature-wise testing. First, by aggregating over vertices in a region and features in a module, we gain statistical power through strength borrowing. If individual features show only moderate associations but ten features in a module all show consistent moderate associations in the same direction, the coherence measure detects this collective signal that individual tests might miss. Second, the cell structure naturally handles multiple testing: we assess $K \times M$ region-module pairs rather than $n \times m$ vertex-feature pairs, dramatically reducing the multiple comparison burden when $K \ll n$ and $M \ll m$. Third, the inference directly addresses the scientific question of interest: which feature modules associate with outcomes in which sample contexts, providing interpretable summaries for downstream mechanistic investigation.

We can extend the inference to compare coherence across cells. For instance, does module S_1 show stronger association with outcome in region R_1 than in region R_2 ? The posterior distribution over differences $\tau(R_1, S_1) - \tau(R_2, S_1)$ quantifies evidence for region-specific effects. Large positive differences with high posterior probability indicate that the module operates differently across regions, while differences indistinguishable from zero suggest the module-outcome relationship is spatially homogeneous.

6.7 Relationship Between Gradient Flow and Co-Monotonicity Cells

The geometric decomposition framework provides two complementary strategies for partitioning the sample space: gradient flow cells based on outcome landscape geometry (Sections 2–3) and co-monotonicity cells based on association profile clustering (Section 6).

These partitions arise from fundamentally different criteria and need not coincide, yet their relationship reveals important insights about the structure of feature-outcome associations.

Gradient flow cells partition vertices based on monotonic behavior of the smoothed outcome \hat{y} . Vertices in the same gradient flow cell lie in a region where \hat{y} varies monotonically from a local minimum to a local maximum, with no intervening extrema. This partition reflects the geometric organization of outcome values in the ambient feature space. In contrast, co-monotonicity cells partition vertices based on similarity of association profiles between outcome and features. Two vertices belong to the same co-monotonicity cell if they have similar co-monotonicity vectors $\widetilde{\text{cm}}(\hat{y}, \hat{Z})$, regardless of their outcome values or position in the gradient flow structure.

When gradient flow and co-monotonicity cells align, the concordance provides strong evidence for a mechanistic interpretation. If gradient flow cell $C(m, M)$ largely overlaps with co-monotonicity region R_j , and if region R_j exhibits strong coherence with feature module S_k , we infer that the features in S_k drive the monotonic outcome variation within cell $C(m, M)$. The outcome increases from minimum m to maximum M because features in module S_k change monotonically along the same gradient paths, and their collective variation explains the outcome behavior. This alignment suggests a causal or mechanistic relationship: the features not only associate with outcomes but do so in a spatially organized manner that respects the geometric structure of the outcome landscape.

Conversely, when gradient flow and co-monotonicity cells disagree, the discordance reveals complexity in the feature-outcome relationships. A single gradient flow cell might span multiple co-monotonicity regions, indicating that different feature modules drive the outcome variation in different parts of the cell. The outcome increases monotonically throughout the cell, but the mechanisms responsible for this increase differ across subregions. Alternatively, a single co-monotonicity region might span multiple gradient flow cells, suggesting that the same feature module associates with outcomes throughout this broader region despite non-monotonic outcome variation within it. Such discordance indicates that association patterns operate at a different spatial scale than outcome gradients, or that multiple compensatory mechanisms produce similar outcomes through different pathways.

The joint analysis of gradient flow and co-monotonicity structures enables more nuanced inference than either approach alone. We can assess whether features in module S_k exhibit different associations within gradient flow cells that intersect co-monotonicity region R_j , testing for context-dependent modulation of associations by outcome level. We can identify features that show strong association throughout a co-monotonicity region spanning multiple gradient cells, suggesting they influence outcomes broadly across different outcome ranges. We can detect regions where outcome gradients are steep but associations weak, indicating that unmeasured features or environmental factors drive the outcome variation.

7. Discussion

We have developed a geometric decomposition framework for statistical inference on high-dimensional structured data, addressing heterogeneous associations through two complementary strategies: gradient flow cells based on outcome geometry, and co-monotonicity

cells based on association profiles. The path monotonicity validation criterion resolves long edge artifacts in discrete gradient flow through geometric verification rather than heuristic thresholding. The co-monotonicity coefficients provide spatially-resolved alternatives to global correlation measures, with derivative weighting connecting to angular correlation of gradients in the continuous manifold limit.

Relationship to Existing Methods

Our framework extends Morse-Smale regression [Gerber et al., 2012] through several key innovations: robust conditional expectation estimation on density-aware Riemannian graphs, systematic spurious extrema removal via prominence filtering and basin overlap clustering, path monotonicity validation for gradient flow edges, and co-monotonicity measures enabling discovery of association-driven structure complementary to outcome-driven partitions.

The framework situates within geometric data analysis rather than topological data analysis. While TDA emphasizes topological invariants like persistent homology that remain unchanged under continuous deformations, our approach focuses on geometric properties like distances, angles, and geodesics dependent on specific metric structure. The Riemannian graphs with vertex and edge masses capture local density and geometry that spectral methods exploit. This geometric emphasis connects our work to manifold learning and spectral graph theory more than to persistent homology.

Limitations and Future Directions

The k -nearest neighbor graph construction introduces discrete approximation of the underlying manifold, with performance sensitive to neighborhood size k . While we employ principled selection based on connectivity and local geometry, adaptive methods that locally vary neighborhood size may improve approximation quality.

Computational scaling presents challenges for very high-dimensional feature spaces. Computing the augmented co-monotonicity embedding requires $O(m^2)$ coefficients for m features, potentially suffering from curse of dimensionality when m is large. Dimensionality reduction through principal component analysis on association profiles or sparse formulations computing only selected inter-feature associations may alleviate this burden.

The current framework applies to continuous or binary outcomes through spectral filtering. Extension to general discrete outcomes (count data, categorical responses) and survival outcomes requires development of appropriate smoothing operators that respect the outcome type while preserving geometric structure.

The framework naturally accommodates multi-modal data integration through co-monotonicity embeddings incorporating associations within and between multiple feature sets. Temporal extensions for longitudinal data could track how co-monotonicity cells evolve over time, while causal inference extensions employing directed graphs could move beyond association to intervention prediction.

Appendix A: Hodge Laplacian Matrix Formula

Derivation of the Hodge Laplacian on chains formula.

The chain Hodge Laplacian on p -chains is defined as

$$L_p = \partial_{p+1}\partial_{p+1}^* + \partial_p^*\partial_p$$

Thus

$$L_p : C_p \rightarrow C_p$$

with

$$\partial_{p+1} : C_{p+1} \rightarrow C_p$$

$$\partial_{p+1}^* : C_p \rightarrow C_{p+1}$$

When inner products are represented by matrices M_p and M_{p-1} , the adjoint takes the matrix form:

$$\partial_p^* = M_p^{-1}\partial_p^T M_{p-1}$$

To derive this, let $\alpha = \sum_i \alpha_i \sigma_i^{(p)}$ and $\beta = \sum_j \beta_j \sigma_j^{(p-1)}$ where $\{\sigma_i^{(p)}\}$ are basis p -simplices. In matrix notation:

$$\langle \partial_p \alpha, \beta \rangle_{p-1} = (\partial_p \boldsymbol{\alpha})^T M_{p-1} \boldsymbol{\beta} = \boldsymbol{\alpha}^T \partial_p^T M_{p-1} \boldsymbol{\beta}$$

$$\langle \alpha, \partial_p^* \beta \rangle_p = \boldsymbol{\alpha}^T M_p (\partial_p^* \boldsymbol{\beta})$$

Equating these for all $\boldsymbol{\alpha}$ gives $M_p (\partial_p^* \boldsymbol{\beta}) = \partial_p^T M_{p-1} \boldsymbol{\beta}$, hence the matrix formula

$$\partial_p^* = M_p^{-1}\partial_p^T M_{p-1}$$

and hence

$$\partial_{p+1}^* = M_{p+1}^{-1}\partial_{p+1}^T M_p$$

Therefore

$$\partial_{p+1}\partial_{p+1}^* = \partial_{p+1} M_{p+1}^{-1} \partial_{p+1}^T M_p$$

and

$$\partial_p^*\partial_p = M_p^{-1}\partial_p^T M_{p-1}\partial_p$$

If we use the matrix notation B_p for ∂_p , then

$$\partial_{p+1}\partial_{p+1}^* = B_{p+1} M_{p+1}^{-1} B_{p+1}^T M_p$$

and

$$\partial_p^*\partial_p = M_p^{-1} B_p^T M_{p-1} B_p$$

Appendix C: Vertex-Level and Path-Based Mutual Information

Given the limitations of global mutual information discussed in Section 4.1, one naturally asks whether MI can be localized to vertices or paths, analogous to the co-monotonicity coefficients developed in this paper. While such localizations are theoretically well-defined, they introduce substantial practical challenges that make them less suitable for the regional inference framework we pursue. We outline two natural constructions and discuss the difficulties that arise in their implementation.

Vertex-Level Mutual Information via Pointwise MI

Mutual information admits a pointwise decomposition that suggests a natural vertex-level measure. For random variables Y and Z with joint density $p(y, z)$ and marginal densities $p(y)$ and $p(z)$, the pointwise mutual information is defined as

$$\text{pmi}(y, z) = \log \frac{p(y, z)}{p(y)p(z)}, \quad (51)$$

with the property that $I(Y; Z) = \mathbb{E}_{Y, Z}[\text{pmi}(Y, Z)]$. To obtain a vertex-level measure, we estimate local densities using kernel weighting centered at each vertex. For vertex $v \in V$, define the kernel-weighted densities

$$p_v(y, z) = \frac{\sum_{u \in V} w_v(u) \cdot K_h((y_u, z_u), (y, z))}{\sum_{u \in V} w_v(u)}, \quad (52)$$

where K_h is a kernel function with bandwidth h and $w_v(u)$ assigns spatial weights based on graph distance or heat kernel diffusion. The marginal densities $p_v(y)$ and $p_v(z)$ are computed similarly. The vertex-level pointwise mutual information is then

$$\text{pmi}_v(Y, Z) = \log \frac{p_v(y_v, z_v)}{p_v(y_v) \cdot p_v(z_v)}, \quad (53)$$

evaluated at the observed values (y_v, z_v) .

This construction yields a scalar measure at each vertex that quantifies how much more (or less) frequently the observed pair (y_v, z_v) occurs in the local neighborhood compared to what independence would predict. High positive values indicate strong local association, negative values suggest local repulsion, and values near zero indicate approximate local independence. The resulting function $\text{pmi} : V \rightarrow \mathbb{R}$ provides spatial resolution comparable to co-monotonicity coefficients.

Path-Based Mutual Information

For a path $\gamma = (\gamma_0, \gamma_1, \dots, \gamma_n)$ in the graph, we can restrict attention to observations along the path and compute mutual information using only these values. Let $\{(y_v, z_v) : v \in \gamma\}$

denote the observed pairs along γ . We estimate the joint and marginal densities from this restricted sample and compute

$$I_\gamma(Y; Z) = \sum_{i,j} p_\gamma(y_i, z_j) \log \frac{p_\gamma(y_i, z_j)}{p_\gamma(y_i) \cdot p_\gamma(z_j)}, \quad (54)$$

where the sums range over bins or unique values in the path sample, and the densities are estimated using standard techniques applied to the path-restricted data. This measure quantifies whether Y and Z exhibit statistical dependence specifically along the trajectory γ , making it natural for gradient flow paths where we seek to characterize monotonic co-variation along trajectories to local extrema.

Practical Challenges

Despite their theoretical appeal, these localized mutual information measures face significant practical obstacles. Density estimation requires adequate sample size within each local region or along each path. For vertex-level PMI, graph neighborhoods may contain too few vertices for reliable kernel density estimation. The resulting estimates exhibit high variance and sensitivity to bandwidth choices, with different kernel parameters potentially yielding qualitatively different spatial patterns.

Path-based mutual information faces analogous challenges. For a path we could estimate densities by aggregating kernel-weighted contributions from neighborhoods around vertices along the path. This requires the same bandwidth selection and sample size considerations as vertex-level estimation, with the additional complexity of combining information across multiple local neighborhoods in a coherent manner. Different weighting schemes for aggregating neighborhood contributions introduce further tuning parameters whose selection affects the resulting measure.

Both approaches require careful treatment of zero or near-zero density estimates, which can produce infinite or undefined pointwise MI values. Regularization strategies such as pseudocount addition or density truncation introduce additional tuning parameters whose selection affects results. The computational cost of kernel density estimation at each vertex, repeated across multiple candidate features, becomes prohibitive for large graphs.

Perhaps most importantly, the resulting measures lack the direct geometric interpretation that co-monotonicity coefficients provide. While MI quantifies statistical dependence through distributional properties, co-monotonicity directly measures whether functions increase or decrease together across graph edges, immediately revealing directional concordance. In applications requiring interpretable biomarkers or predictive features, the edge-based definition offers a directness of interpretation that density-based dependence measures lack.

The co-monotonicity framework sidesteps these difficulties by working directly with function differences across edges rather than estimating underlying distributions. By reducing the problem to weighted sums of edge-wise products, we obtain stable estimates with clear geometric meaning and computational efficiency suitable for large-scale applications. While local MI variants represent legitimate alternatives with their own theoretical merits, the

balance of practical considerations favors the co-monotonicity approach for regional inference in high-dimensional structured data.

References

- [1] Manimozhiyan Arumugam, Jeroen Raes, Eric Pelletier, Denis Le Paslier, Takuji Yamada, Daniel R. Mende, Gabriel R. Fernandes, Julien Tap, Thomas Bruls, Jean-Michel Batto, Marcelo Bertalan, Natalia Borrueal, Francesc Casellas, Leyden Fernandez, Laurent Gautier, Torben Hansen, Masahira Hattori, Tetsuya Hayashi, Michiel Kleerebezem, Ken Kurokawa, Marion Leclerc, Florence Levenez, Chaysavanh Manichanh, H. Bjørn Nielsen, Trine Nielsen, Nicolas Pons, Julie Poulain, Junjie Qin, Thomas Sicheritz-Ponten, Sebastian Tims, David Torrents, Edgardo Ugarte, Erwin G. Zoetendal, Jun Wang, Francisco Guarner, Oluf Pedersen, Willem M. de Vos, Søren Brunak, Joël Doré, and MetaHIT Consortium. Enterotypes of the human gut microbiome. *Nature*, 473(7346):174–180, 2011.
- [2] Mikhail Belkin, Partha Niyogi, and Vikas Sindhwani. Manifold regularization: A geometric framework for learning from labeled and unlabeled examples. *Journal of Machine Learning Research*, 7:2399–2434, 2006.
- [3] Richard Bellman. *Adaptive Control Processes: A Guided Tour*. Princeton University Press, Princeton, New Jersey, 1961.
- [4] Emelie Berglund, Jonas Maaskola, Niklas Schultz, Stefanie Friedrich, Maja Marklund, Joseph Bergensträhle, Firas Tarish, Anna Tanoglidi, Sanja Vickovic, Ludvig Larsson, et al. Spatial maps of prostate cancer transcriptomes reveal an unexplored landscape of heterogeneity. *Nature communications*, 9(1):2419, 2018.
- [5] Gunnar Carlsson. Topology and data. *Bulletin of the American Mathematical Society*, 46(2):255–308, 2009.
- [6] Fan RK Chung and F Chung Graham. *Spectral graph theory*. Number 92 in CBMS Regional Conference Series in Mathematics. American Mathematical Society, 1997.
- [7] William G Cochran. *Sampling techniques*. John Wiley & Sons, New York, 3 edition, 1977.
- [8] Ronald R Coifman and Stéphane Lafon. Diffusion maps. *Applied and computational harmonic analysis*, 21(1):5–30, 2006.
- [9] Inderjit S Dhillon. Co-clustering documents and words using bipartite spectral graph partitioning. In *Proceedings of the seventh ACM SIGKDD international conference on Knowledge discovery and data mining*, pages 269–274, 2001.
- [10] Herbert Edelsbrunner and John L Harer. *Computational topology: an introduction*. American Mathematical Society, 2022.

- [11] Michal A Elovitz, Pawel Gajer, Virginia Riis, Amy G Brown, Michael S Humphrys, Johanna B Holm, and Jacques Ravel. Cervicovaginal microbiota and local immune response modulate the risk of spontaneous preterm delivery. *Nature Communications*, 10(1):1305, 2019.
- [12] Jianqing Fan and Jinchi Lv. A selective overview of variable selection in high dimensional feature space. *Statistica Sinica*, 20(1):101, 2010.
- [13] Charles Fefferman, Sanjoy Mitter, and Hariharan Narayanan. Testing the manifold hypothesis. *Journal of the American Mathematical Society*, 29:983–1049, 2016.
- [14] Jennifer M Fettweis, Myrna G Serrano, J Paul Brooks, David J Edwards, Philippe H Girerd, Hardik I Parikh, Bernice Huang, Tomasz J Arodz, Lavanya Edupuganti, Abigail L Glascock, et al. The vaginal microbiome and preterm birth. *Nature Medicine*, 25(6):1012–1021, 2019.
- [15] Pawel Gajer and Jacques Ravel. Adaptive geometric regression for high-dimensional structured data. *arXiv preprint*, 2025. Submitted November 5, 2025.
- [16] Samuel Gerber, Oliver Rübél, Peer-Timo Bremer, Valerio Pascucci, and Ross T Whitaker. Morse–smale regression. *Journal of Computational and Graphical Statistics*, 22(1):193–214, 2013.
- [17] Peter D. Hoff, Adrian E. Raftery, and Mark S. Handcock. Latent space approaches to social network analysis. *Journal of the American Statistical Association*, 97(460):1090–1098, 2002.
- [18] Yuval Kluger, Ronen Basri, Joseph T Chang, and Mark Gerstein. Spectral biclustering of microarray data: coclustering genes and conditions. *Genome Research*, 13(4):703–716, 2003.
- [19] Owen R Liu and Steven D Gaines. Environmental context dependency in species interactions. *Proceedings of the National Academy of Sciences*, 119(36):e2118539119, 2022.
- [20] László Lovász. Random walks on graphs: A survey. In *Combinatorics, Paul Erdős is Eighty*, volume 2, pages 1–46. János Bolyai Mathematical Society, Budapest, 1993.
- [21] Marston Morse. *The Calculus of Variations in the Large*, volume 18 of *Colloquium Publications*. American Mathematical Society, Providence, RI, 1934.
- [22] Jacques Ravel, Pawel Gajer, Zaid Abdo, G. Maria Schneider, Sara S. K. Koenig, Stacey L. McCulle, Shara Karlebach, Reshma Gorle, Jennifer Russell, Carol O. Tacket, Rebecca M. Brotman, Catherine C. Davis, Kevin Ault, Ligia Peralta, and Larry J. Forney. Vaginal microbiome of reproductive-age women. *Proceedings of the National Academy of Sciences*, 108(Supplement 1):4680–4687, 2011.
- [23] Sam T. Roweis and Lawrence K. Saul. Nonlinear dimensionality reduction by locally linear embedding. *Science*, 290(5500):2323–2326, 2000.

- [24] Rajen D Shah and Jonas Peters. The hardness of conditional independence testing and the generalised covariance measure. *The Annals of Statistics*, 48(3):1514–1538, 2020.
- [25] Alexander J. Smola and Risi Kondor. Kernels and regularization on graphs. In Bernhard Schölkopf and Manfred K. Warmuth, editors, *Learning Theory and Kernel Machines: 16th Annual Conference on Learning Theory and 7th Kernel Workshop, COLT/Kernel 2003*, volume 2777 of *Lecture Notes in Computer Science*, pages 144–158, Berlin, Heidelberg, 2003. Springer.
- [26] Joshua B. Tenenbaum, Vin de Silva, and John C. Langford. A global geometric framework for nonlinear dimensionality reduction. *Science*, 290(5500):2319–2323, 2000.
- [27] Robert Tibshirani. Regression shrinkage and selection via the lasso. *Journal of the Royal Statistical Society Series B: Statistical Methodology*, 58(1):267–288, 1996.
- [28] Cole Trapnell. Defining cell types and states with single-cell genomics. *Genome Research*, 25(10):1491–1498, 2015.
- [29] Cole Trapnell, Davide Cacchiarelli, Jonna Grimsby, Prapti Pokharel, Shuqiang Li, Michael Morse, Niall J. Lennon, Kenneth J. Livak, Tarjei S. Mikkelsen, and John L. Rinn. The dynamics and regulators of cell fate decisions are revealed by pseudotemporal ordering of single cells. *Nature Biotechnology*, 32(4):381–386, 2014.
- [30] Edward Witten. Supersymmetry and morse theory. *Journal of Differential Geometry*, 17(4):661–692, 1982.
- [31] Hui Zou and Trevor Hastie. Regularization and variable selection via the elastic net. *Journal of the Royal Statistical Society: Series B*, 67(2):301–320, 2005.